

Accepted Manuscript

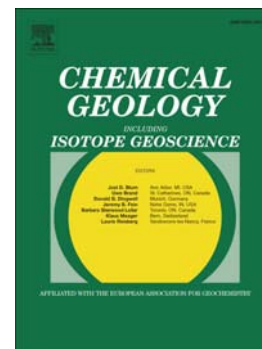
Möwe Bay Dykes, Northwestern Namibia: Geochemical and geochronological evidence for different mantle source regions during the Cretaceous opening of the South Atlantic

Thomas M. Will, Hartwig E. Frimmel, Jörg A. Pfänder

PII: S0009-2541(16)30456-9
DOI: doi: [10.1016/j.chemgeo.2016.08.040](https://doi.org/10.1016/j.chemgeo.2016.08.040)
Reference: CHEMGE 18054

To appear in: *Chemical Geology*

Received date: 11 April 2016
Revised date: 29 August 2016
Accepted date: 31 August 2016



Please cite this article as: Will, Thomas M., Frimmel, Hartwig E., Pfänder, Jörg A., Möwe Bay Dykes, Northwestern Namibia: Geochemical and geochronological evidence for different mantle source regions during the Cretaceous opening of the South Atlantic, *Chemical Geology* (2016), doi: [10.1016/j.chemgeo.2016.08.040](https://doi.org/10.1016/j.chemgeo.2016.08.040)

This is a PDF file of an unedited manuscript that has been accepted for publication. As a service to our customers we are providing this early version of the manuscript. The manuscript will undergo copyediting, typesetting, and review of the resulting proof before it is published in its final form. Please note that during the production process errors may be discovered which could affect the content, and all legal disclaimers that apply to the journal pertain.

Möwe Bay Dykes, Northwestern Namibia: Geochemical and geochronological evidence for different mantle source regions during the Cretaceous opening of the South Atlantic

Thomas M. Will¹, Hartwig E. Frimmel^{1,2}, Jörg A. Pfänder³

¹Institute of Geography and Geology, University of Würzburg, Am Hubland, 97074 Würzburg, Germany

²Department of Geological Sciences, University of Cape Town, Rondebosch 7701, South Africa

³Institute of Geology, TU Bergakademie Freiberg, 09599 Freiberg, Germany

* Corresponding author. Tel.: +49 931 3185418. E-mail address: thomas.will@uni-wuerzburg.de (T.M. Will).

Keywords: Etendeka dykes; NW Namibia; mantle plume; Walvis Ridge; subcontinental lithosphere; Gondwana break-up; South Atlantic opening;

Highlights

- Etendeka dykes in NW Namibia were emplaced over a time span of c. 20 Myr
- Older dykes formed between 135-125 Ma; younger dykes at c. 113 Ma
- Older dykes formed in an off-plume setting during passive rifting
- Younger dykes are derived from the Tristan-Gough plume head
- Younger dykes form the onshore extension of the Walvis Ridge

ACCEPTED MANUSCRIPT

ABSTRACT

Dyke emplacement in the course of Paraná-Etendeka volcanism in northwestern Namibia has been considered as a short-lived event related to a specific magma source at approximately 135-130 Ma. New geochemical, whole rock Sr-Nd-Pb isotope data and $^{40}\text{Ar}/^{39}\text{Ar}$ ages reveal that at least three geochemically and isotopically different tholeiitic dyke generations, with intrusion ages of 135.2 ± 0.7 , 124.1 ± 0.8 Ma and 113.0 ± 0.5 Ma, can be distinguished in the Möwe Bay area, Skeleton Coast of northwestern Namibia. Distinct mantle source components were identified in the petrogenesis of the various dyke generations. Magma composition of the two older dyke suites, both of which were emplaced in a tectonic setting dominated by E-W extension, evolved from a within-plate to an enriched mid-ocean ridge basalt type. Contamination by continental crust and/or lithospheric mantle is suggested by a high $^{238}\text{U}/^{204}\text{Pb}$ -value ($= \mu_{\square}$) of 9.97, which is typical of the Kalahari Craton. The third dyke generation, which intruded in a tectonic regime dominated by SE-NW extension, corresponds to high-Ti ocean island-type basalt with unradiogenic isotopic compositions derived from a mantle source with a μ_{\square} -value of 9.35.

The formation of the older dykes is attributed to the presence of a thermal anomaly in the upper sublithospheric mantle. This anomaly was most likely caused by the peripheral part of a mantle plume that impinged at the base of the lithosphere and caused erosion of the subcontinental mantle lithosphere and melting above the plume head. The initial break-up of SW Gondwana and the formation of early oceanic crust were most likely due to passive rather than active rifting. Continued plume upwelling facilitated by progressive thinning of SW-Gondwana crust led to the formation of the younger, c. 113 Ma old dykes, which are chemically and isotopically

identical to coeval rocks from the northeastern portion of the Walvis Ridge and thus are interpreted as onshore expressions of the Tristan-Gough plume head at that time. The difference in the dominant extension directions of the older and the younger dyke generations can be explained by rotation induced by the Aptian/Albian opening of the Equatorial Central Atlantic, accompanied by a substantial increase in the South Atlantic spreading rate.

1. Introduction

Continental flood basalt and associated intrusive rocks in the Paraná-Etendeka Large Igneous Province formed during Cretaceous rifting of Gondwana, break-up and subsequent opening of the South Atlantic (e.g., Erlank et al., 1984; Turner et al., 1994; Peate, 1997). The resulting passive margin that developed on the eastern side of the South Atlantic is divided by the aseismic Walvis Ridge (Fig. 1a) into a northern and southern segment with marked differences in magmatic, sedimentary and morphological features (e.g., Bolli et al., 1978; Gladczenko et al., 1998; Maystrenko et al., 2013; Koopmann et al., 2014). The Walvis Ridge extends to the continental margin of northwestern Namibia and is considered as the offshore continuation of the Paraná-Etendeka continental flood basalt province (e.g., O'Connor and Duncan, 1990; Renne et al., 1996). The Walvis Ridge has been the target of several drilling, dredging and mapping projects (e.g., Deep Sea Drilling Project Legs 40 and 74; Ocean Drilling Project Leg 208; Walvis Ridge Expedition MV1203; RV Sonne Cruise SO-233) and several geophysical surveys (e.g., Gladczenko et al., 1998; Maystrenko et al., 2013; Koopmann et al., 2014; Fromm et al., 2015). The geochemistry and isotopic composition of Walvis Ridge basalt were studied by various authors (e.g., Bolli et al., 1978; Richardson et al., 1982, 1984; Thompson and Humphris, 1984; O'Connor and Duncan, 1990; Salters and Sachi-Kocher, 2010; O'Connor et al., 2012) as was the timing of volcanism (e.g., O'Connor and Duncan, 1990; O'Connor and le Roux, 1992; O'Connor et al., 2012; Rohde et al., 2013; O'Connor and Jokat, 2015). However, the age and composition of the onshore dykes from the landfall area of the Walvis Ridge have remained poorly studied to date. With the exception of studies by Marsh et al. (2001) and Ewart et al. (2004), which focused mainly on the volcanic rocks, no detailed geochemical and/or isotopic investigation of the co-genetic intrusive rocks around the onshore extension of

the Walvis Ridge have been undertaken. To fill this gap, we targeted dolerite dykes between Terrace Bay and Möwe Bay along the Skeleton Coast in northwestern Namibia (Fig. 1b).

The main objectives of the present study are: (i) to constrain the petrogenesis of dolerite dykes in the Möwe Bay area by means of geochemical and isotope geochemical (whole rock Sr-Nd-Pb) analyses, (ii) to determine the age of emplacement of the dykes by whole rock $^{40}\text{Ar}/^{39}\text{Ar}$ geochronology, (iii) to evaluate the influence of different mantle source regions on the genesis of the rocks, and (iv) to compare the onshore tholeiitic rocks of Möwe Bay with offshore tholeiitic rocks from the Walvis Ridge.

2. Regional geology

The Etendeka volcanic succession on the African side of the South Atlantic is a bimodal suite made up of roughly equal amounts of mafic and felsic volcanic rocks (e.g., Ewart et al., 2004). The Etendeka Province also contains several alkaline to tholeiitic ring complexes, referred to as Damaraland Intrusive Complexes (Ewart et al., 2004), as well as numerous dolerite dykes. It is subdivided into a southern and northern domain, whose boundary coincides with the transition from dominantly high-Ti basalt in the north to low-Ti basalt in the south. According to Marsh et al. (2001), the boundary is located at latitude $19^{\circ}21'$ S, which corresponds to that of the Möwe Bay area (Fig. 1b). Whereas the geochemistry of the extrusive rocks of the Etendeka Province, especially those of the southern subprovince, received considerable attention (e.g., Milner et al., 1995; Erlank et al., 1984; Ewart et al., 1998, 2004; Marsh et al., 2001), the intrusive rocks were investigated in less detail, except for a few studies that focussed on rocks from the Huab (Duncan et al., 1989; Thompson et al., 2001), Horingbaai (Thompson and Gibson, 2000;

Thompson et al., 2001) and the Henties Bay-Outjo areas (Trumbull et al., 2004, 2007; Keiding et al., 2013) in the southern Etendeka Subprovince.

The centre of magmatic activity in the Paraná-Etendeka Large Igneous Province remains highly speculative. Although the areal distribution of volcanic rocks in the Paraná Basin is much larger than in the Etendeka region, the latter was subject to far more erosion due to a more pronounced uplift history of southern Africa. Thus large volumes of volcanic rocks could have been removed from the Etendeka region since Cretaceous times. As the highest spatial density of corresponding mafic dykes, the Hentjesbay-Outjo dyke swarm, and related shallow intrusive ring complexes, the Damaraland Intrusive Complexes, occur along the axis of the Damara Belt further south closer to central Namibia, it may be speculated that this zone represents the most proximal area of volcanic activity. This notion is corroborated by the finding of the maximum crystallisation temperatures being recorded by dykes in the western Hentjes Bay-Outjo dyke swarm some 100 km north of Walvis Bay (Keiding et al., 2013).

The Etendeka dykes at Möwe Bay were emplaced into Neoproterozoic migmatitic paragneisses and granitoids that constitute the basement of the Pan-African Kaoko Belt (e.g., Miller, 2008; Will et al., 2009). More specifically, the host rocks form part of the Coastal Terrane (Goscombe and Gray, 2007), whose voluminous granite bodies can be correlated with the c. 620 Ma Florianópolis Batholith of the Dom Feliciano Belt in Brazil (Konopásek et al., 2016; M.S.A. Basei, unpubl. data). The country rocks represent reworked old cratonic crust, and a palaeogeographic position near the edge of the Kalahari Craton has been suggested (Frimmel et al., 2011; Konopásek et al., 2014). Field relationships indicate that the dykes are either coeval with, or post-date, the flood basalt volcanism (e.g., Miller, 2008 and references therein). Hitherto available geochronological data (mainly Ar-Ar and K-Ar amphibole dating) bracket the timing of

dyke emplacement between 134 and 125 Ma (e.g., Renne et al., 1996; Stewart et al., 1996; Marzoli et al., 1999; Kirstein et al., 2001), which overlaps with available age data for Etendeka basalt and the Damaraland intrusive complexes as summarised by Comin-Chiaramonti et al. (2011). Dyke emplacement was controlled by pre-existing lithospheric discontinuities (Will and Frimmel, 2013). These authors demonstrated that the orientation of the dykes at the west coast of southern Africa extending from Cape Town into southern followed primarily pre-existing basement structures, with the E-W- to NE-SW-directed Cretaceous extension directions being parallel to the Pan-African shortening directions.

Recently geochronological studies of Walvis Ridge samples (Rohde et al., 2013; O'Connor and Jokat, 2015; Hoernle et al., 2015; and references therein) provided unambiguous evidence of a progressive age zonation from 114 Ma at the northeastern end of the Walvis Ridge, which is closest to the Möwe Bay area, to 107-85 Ma in the central portion of the ridge and to 72-58 Ma at the DSDP Leg 74 sites 525A, 527 and 528 near the southwestern end of the Walvis Ridge. There, the Walvis Ridge splits up into two separate subparallel hotspot (sub-)tracks, the Gough and Tristan tracks, that lead to the c. 450 km apart Gough and Tristan da Cunha Islands, respectively (Rohde et al., 2013; Hoernle et al., 2015, 2016). Samples from the two subtracks yielded ages of less than 70 Ma (Rohde et al., 2013). Using Sr-Nd-Pb-Hf isotope data, Hoernle et al. (2015) demonstrated that there is a spatial geochemical zonation of the <70 Ma Gough and Tristan subtracks, with enriched Gough- and a less-enriched Tristan-type compositions. The older (114-72 Ma) segment of the hotspot track extending from near Möwe Bay to the vicinity of the Leg 74 sites has only Gough-type compositions (Hoernle et al., 2015).

3. Petrography and orientation of the Möwe Bay dykes

The dolerite dykes all contain clinopyroxene, plagioclase and opaque phases (mainly ilmenite). In addition, olivine (variably altered to iddingsite) is present in several samples. The rocks have variable grain size ranging from very fine- to coarse-grained and many contain plagioclase and/or clinopyroxene phenocrysts in a fine-grained groundmass.

Three texturally distinct dolerite types can be distinguished in the Möwe Bay area: (i) fine- to medium-grained samples with no or small- to medium-sized plagioclase and/or minor clinopyroxene phenocrysts (Type 1; Fig. 2a), (ii) fine- to medium-grained clinopyroxene- and plagioclase-phyric samples with minor olivine (variably altered to iddingsite, Type 2; Fig. 2b), and (iii) coarse-grained samples with up to several millimetre-long clinopyroxene and/or plagioclase phenocrysts (Type 3; Fig. 2c). Recrystallised clinopyroxene grains that form 120° grain boundary triple junctions and nest-like clinopyroxene aggregates occur in some of the Type 3 sample group (Fig. 2d). Some of the Type 1 samples contain symplectites and/or radially oriented plagioclase or clinopyroxene grains (Figs. 2e and f).

Most of the dykes investigated between Terrace Bay and Möwe Bay (Fig. 1) have coast-parallel NNW-SSE orientations that follow the structural trend of the basement (Will and Frimmel, 2013). In addition, some roughly E-W and NW-SE striking dykes are also present in the area (Fig. 1). The NNW-SSE and E-W striking dykes may form a conjugate set of extension fractures, whereas the NW-SE striking dykes are oriented at an angle of some 30° with respect to the coast-parallel dykes. Noteworthy, Type 1 dykes strike mostly NNW-SSE, Type 2 dykes are generally oriented E-W, whereas the Type 3 dykes strike mainly NW-SE. The dyke orientations

as measured in the field are summarised in Fig. 3; for additional orientation data based on the analysis of satellite images see Will and Frimmel (2013, figs. 4 and 8).

Although limited alteration is evident by variable iddingsitisation of olivine in some samples, the overall degree of alteration is low (most samples have loss on ignition values of well below 1 wt.%; electronic supplement Table S1) and only the least altered samples were selected for further analysis.

4. Geochemistry and isotope compositions

Following the methods outlined by Will et al. (2010), 53 dolerite samples (Table 1) were analysed for major, minor and trace element concentrations (including rare earth elements, REE) at the Department of Geography and Geology, University of Würzburg (XRF) and at the Department of Geological Sciences, University of Cape Town (LA-ICP-MS). The sample locations are indicated in Fig. 1b and the analytical results are summarised in electronic supplement Table S1. Trace element data are presented using the chondrite (cn) and primitive mantle (pm) normalisation values of Sun and McDonough (1989) and McDonough and Sun (1995), respectively. To document the accuracy and precision of the geochemical data, the results of replicate analyses of the international standard that was analysed together with the samples are presented in electronic supplement Table S2. Exemplarily, this table also includes the relative standard deviations (in percent) of some sample analyses.

Whole rock Sm-Nd, Rb-Sr and Pb-Pb isotope data were determined for 32 samples at the Department of Geological Sciences, University of Cape Town, following the procedures described by Will et al. (2010). The whole rock Sm-Nd

isotope data are summarised in Table 2 and the Rb-Sr and Pb-Pb data are presented in Table 3.

Whole rock argon isotope compositions were measured in static mode on a GV Instrument ARGUS noble gas mass spectrometer equipped with five faraday cups at Argonlabor Freiberg (ALF), TU Freiberg, Germany. For analytical details see Appendix A.

4.1. Geochemical classification

In the Pearce (1996) classification diagram all dolerite samples plot in the basalt field (Fig. 4a), whereas in the total alkali versus SiO_2 (TAS) diagram (electronic supplement Fig. S1a) the samples plot in the basalt and basaltic andesite fields. In the SiO_2 versus FeO^*/MgO (FeO^* = total iron as ferrous iron) diagram, all samples plot in the tholeiite field (electronic supplement Fig. S1b).

The SiO_2 concentrations of all samples range from 49 to 54 wt.% and the Mg numbers ($\text{Mg\#} = 100 \cdot \text{molar MgO}/[\text{MgO} + \text{FeO}]$) from 31 to 57. The dolerite samples have moderate to high TiO_2 contents of 0.96 to 2.34 wt.%, with two distinct linear trends if plotted against Mg# (Fig. 4b). The Type 1 and 2 samples define a shallow trend and have variable Mg# numbers, whereas the Type 3 samples plot at intermediate Mg# and high TiO_2 values. The compositional variation of the different dyke suites with respect to MgO as fractionation index is shown in electronic supplement Fig. S2. In addition, the Möwe Bay dolerites are plotted in the Mg# versus Zr/Y diagram (Marsh et al., 2001) showing the various mafic magma types of the Etendeka-Paraná Province (electronic supplement Fig. S3). In contrast to the magma types recognised in the Henties Bay-Outjo dyke swarm of the southern Etendeka Subprovince (Thompson et al., 2001; Trumbull et al., 2007) the Möwe Bay

Type 3 dolerite type have higher TiO_2 for a given MgO value (Fig. S2) and are also distinguished by a distinctly higher Zr/Y ratio (Fig. S3). This dolerite type, referred to as Khumib-type by Marsh et al. (2001), has been suggested to have compositional affinities with the Tristan plume (Ewart et al., 2004).

4.2. Trace element and isotope data

The REE concentrations of all Type 1 samples plot between those of modern ocean island basalt (OIB) and enriched mid-ocean ridge basalt (E-MORB) compositions, those of Type 2 samples plot close to the E-MORB curve, and those of Type 3 are close to the average OIB curve (Figs. 5a, c, e and g).

The Type 1 samples can be further subdivided into two geochemically different subgroups (Types 1a and 1b) by plotting the slope of the light REE, i.e., $(\text{La/Sm})_{\text{cn}}$, versus $(\text{Pb/Pb}^*)_{\text{pm}} = \text{Pb}_{\text{pm}}/\sqrt{(\text{Ce}_{\text{pm}} \cdot \text{Pr}_{\text{pm}})}$, a measure of Pb enrichment and/or depletion (relative to Ce and Pr) in the samples (Fig. 6). The two subgroups have different LREE slopes (Figs. 5a, c and 6) and distinct primitive mantle-normalised trace element patterns (Figs. 5b and d). The $(\text{La/Sm})_{\text{cn}}$ and $(\text{La/Yb})_{\text{cn}}$ ratios of the Type 1a samples range from 1.2 to 1.8 and 1.8 to 2.7, respectively, those of the Type 1b samples have 1.9 to 2.5 and 2.9 to 5.0, respectively (Fig. 6). The Type 2 samples have flat REE patterns ($(\text{La/Sm})_{\text{cn}} = 1.1 - 1.5$; $(\text{La/Yb})_{\text{cn}} = 1.7 - 2.4$), whereas those of Type 3 display relative enrichment in the light REE, with $(\text{La/Sm})_{\text{cn}}$ and $(\text{La/Yb})_{\text{cn}}$ ratios of 1.8 to 2.2 and 3.9 to 6.0, respectively. The Type 1 and 2 samples have rather flat HREE patterns, with $(\text{Gd/Yb})_{\text{cn}}$ ratios ranging from 1.2 to 1.6, whereas the Type 3 samples have slightly higher $(\text{Gd/Yb})_{\text{cn}}$ ratios of 1.7 to 2.2. The LREE concentrations of the Type 1a samples are generally higher than those of the Type

1b samples, which in turn are higher than the Type 2 dolerite LREE concentrations (Fig. 5).

The primitive mantle-normalised element patterns of Types 1a and 1b dolerites are characterised by large positive Pb anomalies, negative Nb, K, P and Ti anomalies and high large-ion lithophile element (LILE) concentrations (Figs. 5b and d). Type 1a dykes have generally higher element concentrations of the elements shown in Fig. 5 than Type 1b and plot close to the upper continental crust curve (Fig. 5b). Type 2 shows weak positive Pb anomalies, negative Nb, P and K anomalies and low LILE concentrations (Fig. 5 f), whereas Type 3 can be distinguished by negative Pb, K and U anomalies (Fig. 5 h). A characteristic feature of all samples is a negative K anomaly of variable extent (Fig. 5). From the REE and the multi-element patterns it appears that the composition of the Type 1 dolerite is intermediate between those of within-plate and enriched mid-ocean ridge basalts, the Type 2 samples have a more enriched mid-ocean ridge composition, and the Type 3 dolerite composition corresponds to high-Ti ocean island basalt with an isotope composition that is similar to that of the enriched mantle 1 (EM 1) end-member reservoir (Fig. 7). In $^{87}\text{Sr}/^{86}\text{Sr}$ versus $^{143}\text{Nd}/^{144}\text{Nd}$ space (Fig. 7a), the majority of the Type 1 and 2 samples define a negative linear trend, with the Type 1a dolerites having the lowest Nd and highest Sr ratios of the Type 1 and 2 samples. The high $^{87}\text{Sr}/^{86}\text{Sr}$ ratios of the Type 1a dolerite samples might be explained by contamination in the subcontinental lithospheric mantle (SCLM) and/or lower crust before assimilation of upper crustal material (e.g., Thompson et al., 2007). The high-Ti Type 3 samples do not plot along this trend but have distinctly lower and uniform Nd and Sr isotope ratios (Fig. 7a). In an uranogenic Pb isotope diagram (Fig. 7b), the Type 1 and 2 samples define a linear array, which is typical of co-genetic samples that had identical Pb composition at some time in the

past. In contrast, the Type 3 samples are distinctly less radiogenic and have rather uniform $^{206}\text{Pb}/^{204}\text{Pb}$ and $^{207}\text{Pb}/^{204}\text{Pb}$ ratios that plot on top of the Walvis Ridge compositional field close to the EM 1 end-member composition. Thus, the Type 1 and 2 samples appear to be co-genetic and must have had an identical Pb composition at some time in the past. Best-fit straight lines through the data yielded μ_2 -value ($\mu_2 = ^{238}\text{U}/^{204}\text{Pb}$) of 9.97 for both Type 1 and 2 samples but a distinctly lower value of 9.35 for the Type 3 dolerite samples. The high μ -value of the former points to a source that was enriched in Th and U compared to that of the Type 3 rocks and, in addition, indicates a greater contribution of crustal Pb to the compositions of Types 1 and 2 than to that of the Type 3 dolerites. This points to derivation from different mantle source regions of the Type 1 and 2 compared to the Type 3 dolerites. It is interesting to note that the Walvis Ridge samples with Gough-type composition (Hoernle et al., 2015) plot on a straight line between our samples (Fig. 7b). This might be interpreted to indicate a similar source region of all of our samples and the Walvis Ridge samples with Gough-type compositions. However, given the age differences between our samples (see below) and the 107-72 Ma old Walvis Ridge samples this interpretation appears unlikely. Even though the enriched ε_{Nd} initials of -7 to -8 of the Type 3 samples (Table 2) point to contamination, all other geochemical (see section 6) and isotope data are consistent with only little contamination by the continental crust of these samples.

5. $^{40}\text{Ar}/^{39}\text{Ar}$ age data

Six fresh, effectively unaltered tholeiitic dyke samples, representing each dolerite type, were selected for whole rock $^{40}\text{Ar}/^{39}\text{Ar}$ dating. The results obtained are summarised in Table 4 and shown in Fig. 8. The full data set is given in the electronic

supplement Table S3. All reported errors are given as 1σ , following the data reporting norm of Renne et al. (2009).

5.1 Type 1 dolerite

Samples *N11-5a*, *N11-9a*, *N11-20*, and *N11-17* were selected as most representative of the Type 1. Sample *N11-5a* produced a slightly hump-shaped age spectrum, with an all-step inverse isochron age of 133.7 ± 2.6 Ma (initial $^{40}\text{Ar}/^{36}\text{Ar} = 297.3 \pm 5.9$). Steps 5 -12 yield a good correlation in an inverse isochron diagram (MSWD = 3.4) with an age of 135.6 ± 1.7 Ma and an initial $^{40}\text{Ar}/^{36}\text{Ar} = 302.4 \pm 4.6$, with possibly a very minor excess Ar component. In contrast, steps 13 - 18 give a somewhat lower inverse isochron age of 131.8 ± 5.4 , at an initial $^{40}\text{Ar}/^{36}\text{Ar}$ of 288 ± 34 . Correcting steps 5 - 12 with an initial $^{40}\text{Ar}/^{36}\text{Ar}$ of 302.4 provides a weighted mean age (WMA) of 135.2 ± 0.7 , which is within error to the all-step inverse isochron age of 133.7 ± 2.6 Ma. The WMA for steps 5 - 12 is therefore taken as best age constraint for this sample.

The age spectrum of sample *N11-9a* appears slightly disturbed due to some, probably weathering-induced Ar loss. This is evident from the inverse isochron plot (Fig. 8), an initial $^{40}\text{Ar}/^{36}\text{Ar}$ of 267.5 ± 7.9 , and an errorchron 'age' of 133.1 ± 2.8 Ma. No contiguous set of temperature steps could be obtained to provide a near-atmospheric $^{40}\text{Ar}/^{36}\text{Ar}$ intercept. Although the age obtained is within error of that of the previous sample, its geological significance is less reliable.

Stepwise heating of sample *N11-20* produced a plateau between steps 6 to 15, with a calculated WMA of 130.5 ± 0.3 Ma. The inverse isochron age for these steps is with 130.2 ± 1.4 Ma identical and yields an initial $^{40}\text{Ar}/^{36}\text{Ar}$ of 304 ± 15 , which is

within error identical to the atmospheric value. The other steps (corresponding to lower apparent ages) most likely reflect limited post-magmatic Ar loss. Thus, the above WMA, which takes into account 60 % of ^{39}Ar released (Fig. 8), is regarded as best approximating the true age of this sample.

Sample *N11-17* did not yield a plateau but progressively increasing apparent ages (Fig. 8), and a sub-atmospheric initial $^{40}\text{Ar}/^{36}\text{Ar}$ ratio of 243.9 ± 7.2 for all steps. All of this points to significant Ar loss. Inverse isochron plots of contiguous steps that provide linear correlations with low MSWD (steps 10 - 14, 14 - 21, 17-21) yield ages between ~130 and ~126 Ma. Given the sub-atmospheric initial $^{40}\text{Ar}/^{36}\text{Ar}$ ratios (~260 and ~286), these ages are considered less reliable than the above WMA's.

5.2 Type 2 dolerite

Sample *N11-21* was taken from a dyke that cross-cuts that from which sample *N11-20* was taken and, consequently, must be younger. It yielded an age pattern with low apparent ages for the initial low-temperature steps (Fig. 8) and sub-atmospheric initial $^{40}\text{Ar}/^{36}\text{Ar}$ of 279.9 ± 8.1 (calculated from all steps), from which some Ar loss is inferred. However, steps 5 – 16, which represent 92% of all ^{39}Ar released, yielded a well-defined plateau that corresponds to a WMA of 124.1 ± 0.8 Ma (Fig. 8). The inverse isochron age for these steps (126.3 ± 4.5 Ma) is identical within error, and the initial $^{40}\text{Ar}/^{36}\text{Ar}$ is indistinguishable from the atmospheric ratio (298.6 ± 0.3 ; Lee et al., 2006). Consequently, the WMA is taken as best age constraint for this sample.

5.3 Type 3 dolerite

Sample *N11-13* is the most representative fresh example of Type 3 dolerite. It yielded an almost perfect plateau, except for the first few steps (Fig. 8). The plateau defined by steps 4 - 20, representing 97.3% of the total ^{39}Ar released, corresponds to a WMA of 113.0 ± 0.5 Ma. The initial $^{40}\text{Ar}/^{36}\text{Ar}$ ratio of these steps in an inverse isochron plot is 298.6 ± 2.4 , which is identical to the atmospheric value (298.6 ± 0.3 ; Lee et al. 2006), and the WMA. The WMA is thus regarded as precise age estimate for this sample.

6. Interpretation and discussion

6.1. Degree of melting

The relatively evolved nature of all dolerite dykes in the Möwe Bay area ($\text{MgO} \leq 8.1$ wt.%; $\text{Ni} < 180$ ppm, $\text{Cr} < 320$ ppm) indicates that even the least evolved dykes (Type 2) do not represent an unfractionated primary magma but formed from an already differentiated magma source and/or differentiated during ascent. The REE patterns of the various dolerite type samples have nearly parallel trends and are variably enriched in the LREE relative to the HREE (Figs. 5a, c, e and g), which show only very little or moderate fractionation $(\text{Tb}/\text{Yb})_{\text{cn}} 1.1\text{-}1.4$ and $1.4\text{-}1.8$ of the Type 1 and 2 and the Type 3 dolerite dykes, respectively. This could point to absence of residual garnet and indicating melting at shallow depths within the spinel-peridotite stability field or, alternatively, could also be attributed to large degrees of melting at greater depths. The latter interpretation is more probable because even the most mafic but still slightly fractionated Type 2 tholeiitic dykes have E-MORB-like REE abundances with only very slight HREE fractionation, being consistent with large degrees of melting. Thus, little residual garnet is likely to reflect large degrees of partial melting and not necessarily melting of a shallow source. The moderately

fractionated middle to heavy REE of the Type 3 dykes may be due to involvement of garnet in fractionating these elements, i.e., formation of these rocks could have occurred in the garnet-peridotite stability field (e.g., Class et al., 1998) or, alternatively, the parental melts of the Type 3 dykes may have been generated within the spinel-garnet transition zone by the complete melting of garnet.

The Th/Yb and Nb/Yb ratios of the samples are reliable proxies of the amount of melting (or for the involvement of crustal material; see below), with high values indicating low degrees of melting (Pearce and Peate, 1995). If true, the older dykes might have experienced a progressively decreasing amount of partial melting from Type 1a to 1b and to Type 2 with time (Fig. 9a). From the data it is not possible to determine whether the Type 3 parental magmas experienced a different degree of partial melting than the Type 1 and 2 magmas (Fig. 9a) nor is it clear whether they formed in different mantle facies, e.g., in the spinel- or garnet-peridotite stability field. Irrespective of these uncertainties, from the isotopic data (Fig. 7) it is clear that the older and younger dyke types must have been derived from melts that formed in distinctly different mantle source regions. The Walvis Ridge samples (Salters and Sachi-Kocher, 2010; Hoernle et al., 2015) define a trend that is subparallel to the E-MORB—OIB array and includes the Möwe Bay Type 3 samples (Fig. 9a).

6.2. Crustal and/or lithospheric contamination

Low $(\text{Nb}/\text{Nb}^*)_{\text{pm}}$ ($= \text{Nb}_{\text{pm}}/\sqrt{(\text{Th}_{\text{pm}} \cdot \text{La}_{\text{pm}})}$) values are, like high Th/Ta and Th/Yb ratios, considered to be reliable proxies for the involvement of crustal material in the petrogenesis of basaltic rocks (e.g., Pearce and Peate, 1995; Riley et al., 2005). Plotting $(\text{Nb}/\text{Nb}^*)_{\text{pm}}$ against MgO shows a weak positive correlation in the case of the Type 1 and 2 dykes (Fig. 9b). The $(\text{Nb}/\text{Nb}^*)_{\text{pm}}$ ratios of Type 1 samples are low,

whereas the Type 2 samples have slightly higher values and the Type 3 samples have the highest $(\text{Nb}/\text{Nb}^*)_{\text{pm}}$ ratios of all samples. The latter are in the range of those values advocated for the EM1 and 2 and the primitive mantle end-members (McDonough and Sun, 1995). Thus, it appears that the different dyke types were variably contaminated by continental crust, with the Type 1a samples having experienced the largest and the Type 3 dykes the least contamination. The same conclusion is reached from the data shown in Fig. 9a. The oldest samples (Type 1a) have the highest Nb/Yb and Th/Yb ratios and were more strongly contaminated than the younger Type 2 samples and yet younger Type 3 samples. In addition, it is likely that high LREE/HREE ratios of the Type 1 and 2 dykes (Figs. 5 and 6) and high (e.g., Th/Yb, Th/Nb and Ba/Nb) and low (e.g., $(\text{Nb}/\text{Nb}^*)_{\text{pm}}$, Ce/Pb) incompatible element ratios (Fig. 9 and electronic supplement Table S1) are largely due to assimilation of and contamination by upper continental crust that was probably part of the Kalahari Craton (see below). It is noteworthy, that the $(\text{Nb}/\text{Nb}^*)_{\text{pm}}$ ratios of the Type 3 dykes (Figs. 9b and c) overlap with the lower end of the compositional range of the Walvis Ridge samples investigated by Salters and Sachi-Kocher (2010) and Hoernle et al. (2015). This might indicate that the Type 3 tholeiitic dykes experienced a higher degree of lower crustal assimilation than most of the Walvis Ridge samples or, alternatively, it could point to melt contamination by enriched lithospheric mantle.

The high $^{207}\text{Pb}/^{204}\text{Pb}$ and $^{206}\text{Pb}/^{204}\text{Pb}$ ratios of the Type 1 and Type 2 samples are typical of contamination and/or assimilation of old continental crust in their petrogenesis. The Type 1 and 2 dykes formed in a mantle reservoir with a second-stage μ_2 -value (Fig. 7b) that corresponds to that of the Kalahari Craton (Frimmel et al., 2004; Jung et al., 2012). Figure 7c shows that all Möwe Bay Type 1 and 2 samples plot on a best-fit straight line that extends through the Pb isotopic

composition of the Kalahari Craton from Jung et al. (2012). This is interpreted to indicate (i) that the Type 1 and 2 samples are cogenetic and (ii) that mixing between the Kalahari Craton and the Type 1 and 2 doleritic melts occurred during Early Cretaceous dyke emplacement. The involvement of ancient material in the formation of these rocks is further supported by the fact that the best-fit straight line of the Type 1 and 2 samples intersects the modelled Pb evolution curve ($\mu_2 = 9.97$) at c. 1770 Ma (electronic supplement Fig. S4). This Eburnean age corresponds to ~1770 Ma old protolith ages in the neighbouring Kaoko Belt (Seth et al., 1988) and close to c. 1800 Ma old zircon provenance data for the Congo Craton (Konopásek et al., 2014).

Correlations of $^{143}\text{Nd}/^{144}\text{Nd}$ and $^{87}\text{Sr}/^{86}\text{Sr}$ with Ce/Pb (electronic supplement Fig. S5) also indicate that the Type 1 and 2 dolerite dykes were strongly affected by assimilation of continental crustal material, whereas the Type 3 dykes seem to have experienced considerably less contamination. We interpret these data to indicate that the E-MORB-type parental magmas of the Type 1 and 2 dykes were contaminated by the Kalahari Craton, with the amount of contamination decreasing from the older Type 1a to the younger Type 2 dyke generations. The yet younger Type 3 dykes experienced the least crustal contamination of all Möwe Bay dolerite samples.

6.3. Possible source regions

Analogous to the weakly fractionated HREE of the Möwe Bay samples (Fig. 5) their negative K anomalies could also be interpreted to point to a shallow magma source region in the SCLM. Negative K anomalies in alkaline rocks have been explained by the presence of residual amphibole in the source region (e.g., Späth et al., 2001). While amphibole is unstable in both the convecting asthenospheric upper mantle and in asthenospheric mantle plumes, it can be stable in old SCLM (Class

and Goldstein, 1997). Residual amphibole, however, is unlikely to survive if tholeiitic melts form by high degrees of partial melting. K-bearing phases such as phlogopite or richterite are very fusible and if they are to be retained in the source region the amount of partial melting would have to be considerably lower than the melt fraction required to form the E-MORB composition of the tholeiitic Type 1 and 2 dolerites in the Möwe Bay area. It is therefore more likely that, by analogy with many Walvis Ridge samples (e.g., Salters and Sachi-Kocher, 2010; Hoernle et al., 2015), the negative K-anomaly is not related to the presence of a residual K-bearing phase but reflects a source characteristic of the upper sublithospheric mantle.

The $(\text{Ce/Pb})_{\text{pm}}$ and $(\text{Tb/Yb})_{\text{pm}}$ ratios of the Type 1 and 2 samples are lower and the Ba/Nb ratios higher than those of the Type 3 rocks (Figs. 9 c-e). The compositions of the Type 3 samples overlap with those of the Gough-type samples from the Walvis Ridge (Salters and Sachi-Kocher, 2010; Hoernle et al., 2015). These geochemically enriched Walvis Ridge samples are interpreted by these authors to be plume-derived, which is, by analogy, most likely also the case for the Möwe Bay Type 3 dolerite samples. This is further supported by the high $(\text{Ce/Pb})_{\text{pm}}$ and $(\text{Tb/Yb})_{\text{pm}}$ ratios of these rocks, which are - like those of the Walvis Ridge samples - close to or higher than average global values sometimes invoked to discriminate between plume- and non-plume-derived melts (e.g., Wang et al., 2002; Tian et al., 2010). In addition, le Roex et al. (2010) demonstrated that plume-related samples have consistently lower Ba/Nb ratios compared to those that formed by melting of recycled, metasomatised southern African SCLM. As obvious from Fig. 9e the Ba/Nb ratios of our Type 1 and 2 samples range between 17 and 28, with the majority of the samples having values of c. 25, whereas the Type 3 samples have much lower Ba/Nb ratios of 14 - 19, which overlap with those of the Walvis Ridge samples.

However, assimilation of continental crust, which clearly affected the source area of Type 1 and 2 samples (see above) lowers the $(\text{Tb/Yb})_{\text{pm}}$ and $(\text{Nb/Nb}^*)_{\text{pm}}$ and increases the Ba/Nb ratio. Thus, it cannot be excluded that the parental melts of the older dykes are also plume-related but subsequent assimilation of crustal and/or lithospheric material may have obliterated the evidence thereof.

From Fig. 7b it is evident that the Type 1 and 2 samples do not plot near the Tristan da Cunha and/or Walvis Ridge compositional fields, whereas the Pb isotopic composition of the Type 3 samples is identical to that of Walvis Ridge tholeiite. Again, this indicates that different source regions were involved in the genesis of the different dolerite types. Similarities in source are, however, obvious for the basaltic rocks that make up the Walvis Ridge and the c. 113 Ma old Möwe Bay Type 3 dykes.

6.4. Timing of dyke emplacement

Although limited in numbers, our new Ar-Ar age data, especially those obtained on samples least affected by Ar loss, strongly point at a prolonged period of dyke emplacement in the study area - much longer than previously envisaged. The fact that texturally different dykes with partly different orientations in the field are not only geochemically distinctly different but also yielded different ages suggests that they represent different dyke generations that were derived from different sources and emplaced at different times. Invariably, an Ar-Ar age represents a cooling age rather than a magmatic crystallization age. The difference between the two age types should be, however, small in the case of a dyke emplaced at shallow crustal level. Even if a comparatively coarser grain size of one type of dyke might imply a somewhat slower cooling history, it fails to explain the remarkable differences in Ar-Ar ages obtained in this study for the different dolerite types. Thus, we interpret the

available age and lithogeochemical data as reflecting several generations of dykes: The oldest is Type 1 for which the most reliable Ar-Ar age data range between 135.2 ± 0.7 Ma and 130.5 ± 0.3 Ma. A younger age for the Type 2 dykes is indicated by field observations as they cross-cut Type 1 dykes in places. This is supported by the limited Ar-Ar age date with the best available age constraint for Type 2 being 124.1 ± 0.8 Ma. Thus, the Type 1 and 2 dykes intruded within a time span of c. 9 - 10 Myr. The best age constraint for the Type 3 dyke is 113.0 ± 0.5 Ma. Despite the limited number of samples dated, we expect by analogy with geochemically and isotopically similar Type 3 dykes (Figs. 5, 6 and 7) that many more dykes in the Möwe Bay area were emplaced at that time. The age of the Type 3 dyke is identical to the oldest samples from the Walvis Ridge, which provided Ar-Ar ages of 114 - 112 Ma (Rohde et al., 2013). As recently shown by Rohde et al. (2013), O'Connor and Jokat (2015) and Hoernle et al. (2015) there is a continuously younging age progression from 114 Ma at the northeastern end of the Walvis Ridge, which is closest to the Möwe Bay area to 107-85 Ma between latitude 22° and 27° S and to 72-58 Ma at the DSDP Leg 74 sites 525A, 527 and 528 near the southwest end of the Walvis Ridge. There, the Walvis Ridge splits up into two separate hotspot tracks (Tristan and Gough tracks) from which younger ages of less than 70 Ma have been obtained (Rohde et al., 2013).

6.5. *Geodynamic implications*

The geochemical and isotope data presented above provide evidence for the Möwe Bay dykes having originated in distinctly different mantle source areas. The parental melts of the older Type 1 and 2 dykes are interpreted to have formed in an off-plume setting on top of a thermal anomaly in the upper asthenospheric mantle. We interpret this anomaly as the distal part of a plume head that impinged at the

base of the lithosphere, caused erosion of the overlying SCLM and triggered partial melting there. Thus, thermal erosion of the Gondwana SCLM might have caused asthenospheric melting at depths corresponding to the spinel-peridotite stability field during the formation of the older dykes (e.g., Gibson et al., 2005). Subsequently, the Type 1 and 2 dykes were extensively contaminated in the continental lithosphere. In contrast, the parental melts of the younger, c. 113 Ma old Type 3 samples probably experienced less upper crustal contamination than the older dykes and are interpreted to be derived from the Tristan-Gough plume head that must have caused massive asthenospheric melting in the mantle beneath NW Namibia at that time. These rocks are chemically and isotopically identical to 114-112 Ma old mafic rocks with enriched Gough-type compositions from the northeastern end of the Walvis Ridge (Rohde et al., 2013; Hoernle et al., 2015) and are therefore regarded as the onshore extension of the Walvis Ridge.

Our interpretation that the intrusion of the older dykes in the Möwe Bay area occurred in a distal plume setting, in which no significant amount of underplating occurred is consistent with results of recent geophysical studies from the Walvis Ridge and its landward continuation (Ryberg et al., 2015; Fromm et al., 2015) and other locations along the South Atlantic margins (e.g., Koopmann et al., 2014; Becker et al., 2016). The geophysical surveys of the Walvis Ridge did not find evidence of massive underplating at and near the NW Namibian coast and, hence questioned the active role of a mantle plume during SW Gondwana break-up in this area but suggested a passive rifting environment. Passive rifting commonly follows pre-existing lithospheric anisotropies. This was demonstrated to have been crucial during the initial break-up of Gondwana (Frimmel et al., 2011, 2013; Will and Frimmel, 2013; Will et al., 2014). Using structural, geochemical and isotope data these authors

showed that break-up was most likely controlled by far-field forces and followed pre-existing lithospheric anisotropies. In the case of the South Atlantic this was the long axis of a former back-arc basin that formed on top of a thinned and thermally weakened lithosphere and which closed at Ediacaran times during the final stages of the Pan-African/Brasiliano orogeny. Thus all the geophysical, structural and geochemical studies referred to above point to passive rather than active rifting leading up to Gondwana break-up and the formation of early oceanic crust.

Our data and interpretation do not contradict earlier studies that suggest the presence of a wide plume head in the present-day South Atlantic region at c. 135-130 Ma (e.g., Thompson and Gibson, 2000; Gibson et al., 2005; Thompson et al., 2007; Trumbull et al., 2007; Hoernle et al., 2015; and references therein). While our data indeed suggest little direct plume melting and underplating during the formation of the Type 1 and 2 dykes in the Möwe Bay area in NW Namibia, they do not disprove the existence of a broad plume head at that time but they suggest that the parental melts of the Type 1 and 2 dyke generations were derived from above or adjacent to the plume head. The centre of massive underplating and asthenospheric melting, required to explain the extensive Paraná-Etendeka flood basalt province and related dykes is suspected further south at, or close to, the Hentjes Bay-Outjo dyke swarm in west-central Namibia (e.g., Thompson and Gibson, 2000; Trumbull et al., 2007; Gibson et al., 2005, 2006; Keiding et al., 2013; Hoernle et al., 2015; and many more).

Our new Ar-Ar data show that the Type 1 and 2 dykes intruded during a time span of c. 9-10 Myr. This agrees with recent geomagnetic data that require a minimum period of Etendeka volcanic activity of at least 4 - 5 Myr (Dodd et al., 2015) instead of the previously thought brief time span of c. 2 Myr or even less (Renne et al., 1996;

Janasi et al., 2011). Our age data not only provide evidence of a prolonged period of Etendeka volcanism but also corroborate the conclusion reached by Dodd et al. (2015) that the long volcanic activity and the lack of changes in its rates may explain the absence of mass extinction events during the Cretaceous Paraná-Etendeka volcanism.

The dominant extension directions for the emplacement of the older and the younger dyke generations differ by approximately 30°, which is probably due to plate rotations induced by the opening of the Equatorial Central Atlantic at the Aptian/Albian boundary. It may be speculated that this opening is related to a substantial increase in spreading rate from c. 3-4 cm/yr to 8 cm/yr or even more in the South Atlantic (Colli et al., 2014) at that time. Additionally, the Aptian/Albian boundary marks the onset of sea-floor spreading north of the Walvis Ridge (Torsvik et al., 2009), the start of dissecting once coherent syn-rift salt basins in the South Atlantic (Moriak et al., 2008) and the final separation of South America and Southern Africa in the Santos-Benguela margin segment (Heine et al., 2013). Thus, the emplacement of plume-related Type 3 dykes in northwestern Namibia occurred contemporaneously with several large-scale geological changes and plate boundary re-arrangements in the present-day South Atlantic region.

7. Conclusions

New geochemical, whole rock Sr, Nd and Pb isotope and Ar-Ar age data for tholeiitic dykes from the Möwe Bay area in the Etendeka Province in northwestern Namibia make it possible to draw a number of conclusions:

1. The Möwe Bay area contains at least three texturally, geochemically and isotopically different tholeiitic dyke generations, a feature that is not present to the

south or north of Möwe Bay in such a limited geographical area. The geochemical and isotope data indicate that the Möwe Bay dykes originated in distinctly different mantle source areas.

2. The emplacement age of the dykes range from 135.2 ± 0.7 Ma to 113.0 ± 0.5 Ma. The older dykes (Types 1 and 2) intruded between 135.2 ± 0.7 Ma and 124.1 ± 0.8 Ma (Valanginian to Barremian), the younger dykes (Type 3) intruded at around 113.0 ± 0.5 Ma (Aptian/Albian boundary). The older dykes intruded during a time span of c. 9-10 Myr indicating a substantially longer period of Paraná-Etendeka volcanic activity than previously thought (e.g., Renne et al., 1996; Janasi et al., 2011) but in agreement with recent geomagnetic data (Dodd et al., 2015).

3. The composition of the Type 1 dolerite is intermediate between within-plate and enriched mid-ocean ridge basalts, whereas Type 2 samples have a more enriched mid-ocean ridge basalt composition. Both dolerite suites share a high μ_2 -value of 9.97 and were extensively contaminated. The parental magmas of these dykes are interpreted to have formed in a distal plume setting on top of a thermal anomaly in the upper sublithospheric mantle without massive underplating. The plume impinged at the base of the lithosphere and provided enough thermal energy to heat the overlying Gondwana SCLM and caused its partial melting. Hence, an active role of the plume during initial Gondwana break-up and opening of the South Atlantic in NW Namibia is questionable.

4. The younger Type 3 dolerite are high-Ti ocean island basalt that experienced less contamination by the continental crust and/or the metasomatised SCLM from underneath southwestern Africa than the older dykes. The parental melts are interpreted to be derived from the Tristan-Gough plume head. The samples have

unradiogenic Nd, Pb and Sr isotopic compositions and formed in a mantle domain with a μ_2 -value of 9.35. The 113 Ma old type 3 dolerites are chemically and isotopically identical to coeval mafic rocks from the northeastern end of the Walvis Ridge and are considered as the onshore extension of the Walvis Ridge.

5. The Aptian/Albian intrusion age of ~113 Ma of the Type 3 dykes is coeval with several major tectonic events in the South and Central Atlantic, including the initiation of sea-floor spreading north of the Walvis Ridge, and a substantial increase in spreading rate that is attributed to interrelated changes in horizontal plate motion and vertical motion in the surrounding continents (Colli et al., 2014).

6. The Type 1 and 2 dykes form a conjugate pair with a dominant NNW-SSE-directed orientation, whereas the younger Type 3 dykes are mainly oriented NW-SE, indicating that the latter orientation dominated during the later stages of continental break-up. Thus, there was a progressive change in extension directions from a generally E-W to NE-SW orientation with time. It can be speculated that this difference in orientation of c. 30°, which is also evident between dykes from SW Angola and the Skeleton Coast in NW Namibia (Will and Frimmel, 2013), is due to the rotation induced by the Aptian/Albian opening of the Equatorial Central Atlantic. Such a causal link between changes in extension directions and plate velocities over time appears very likely.

Acknowledgements

We thank U. Schüssler for his help with the XRF analyses and P. le Roux for whole rock trace element and isotope analyses. D. Brachmann and B. Sperner are thanked for supporting the Ar-Ar analyses. Michal Kolečka and the team from the Reactor Services Division of the Nuclear Research Centre in Řež, Czech Republic, are

acknowledged for the neutron irradiation of the samples. We also thank the Geological Survey of Namibia for providing access to restricted areas in the Skeleton Coast Park. This study was supported by grants from the Deutsche Forschungsgemeinschaft (Wi 1225/5 and FR 2183/8) within the priority program SAMPLE (South Atlantic Margin Processes and Links with Onshore Evolution, SPP 1375). Comments on an earlier version of the manuscript by E.S. Jennings and S. Gibson are highly appreciated as well as the very constructive reviews by S. Jung, R. Trumbull and an anonymous reviewer.

References

- Becker, K., Tanner, D.C., Franke, D., Krawczyk, C.M., 2016. Fault-controlled lithospheric detachment of the volcanic southern South Atlantic rift. *Geochemistry, Geophysics, Geosystems* 17, doi: 10.1002/2015GC006081.
- Bolli, H.M. and 12 others, 1978. Walvis Ridge-sites 362 and 363. Initial Repts. Deep Sea Drill. Proj. 40, 183-356.
- Class, C., Goldstein, S.L., 1997. Plume-lithosphere interactions in the ocean basins: constraints from the source mineralogy. *Earth Planet. Sci. Lett.* 150, 245-260.
- Class, C., Goldstein, S.L., Altherr, R., Bachèlery, P., 1998. The process of plume-lithosphere interactions in the ocean basins - the case of Grande Comore. *J. Petrol.* 39, 881-903.
- Colli, L., Stotz, I., Bunge, H.-P., Smethurst, M., Clark, S., Iaffaldano, G., Tassara, A., Guillocheau, F., Bianchi, M.C., 2014. Rapid South Atlantic spreading changes and coeval vertical motion in surrounding continents: evidence for temporal changes of pressure-driven upper mantle flow. *Tectonics* 32, 1304-1321.
- Comin-Chiaramonti, P., De Min, A., Girardi, V.A.V., Ruberti, E., 2011. Post-Paleozoic magmatism in Angola and Namibia: a review. In: Geological Society of America, Special Papers vol. 478, 223-247.
- Dodd, S.C., Niocaill, C.M., Muxworthy, A.R., 2015. Long duration (>4 Ma) and steady-state volcanic activity in the early Cretaceous Paraná-Etendeka large igneous province: new palaeomagnetic data from Namibia. *Earth Planet. Sci. Lett.* 414, 16-29.
- Duncan, A.R., Newton, S.R., van den Berg, C., Reid, D.L., 1989. Geochemistry and petrology of dolerite sills in the Huab River Valley, Damaraland, north-western Namibia. *Communs. Geol. Surv. Namibia* 5, 5-18.
- Erlank, A.J., Marsh, J.S., Duncan, A.R., Miller, R.M., Hawkesworth, C.J., Betton, P.J., Rex, D.C., 1984. Geochemistry and petrogenesis of the Etendeka volcanic rocks from SWA/Namibia. *Spec. Publ. Geol. Soc. South Afr.* 13, 195-245.
- Ewart, A., Milner, S.C., Armstrong, R.A., Duncan, A.R., 1998. Etendeka volcanism of the Goboboseb Mountains and Messum Igneous Complex, Namibia. Part I: geochemical evidence of Early Cretaceous Tristan plume melts and the role of crustal contamination in the Paraná-Etendeka CFB. *J. Petrol.* 39, 191-225.
- Ewart, A., Marsh, J.S., Milner, S.C., Duncan, A.R., Kamber, B.S., Armstrong, R.A., 2004. Petrology and geochemistry of Early Cretaceous bimodal flood volcanism of the NW

- Etendeka, NW Namibia. Part 1: Introduction, mafic lavas and reevaluation of mantle source components. *J. Petrol.* 45, 59-105.
- Frimmel, H.E., Jonasson, I.R., Mubita, P., 2004. An Eburnean base metal source for sediment-hosted zinc-lead deposits of Namibia: lead isotopic and geochemical evidence. *Mineral. Dep.* 39, 328-343.
- Frimmel, H.E., Basei, M.S., Gaucher, C., 2011. Neoproterozoic geodynamic evolution of SW-Gondwana: a southern African perspective. *Int. J. Earth Sci.* 100, 323-354.
- Frimmel, H.E., Basei, M.A.S., Correa, V.X., Mbangula, N., 2013. A new lithostratigraphic subdivision and geodynamic model for the Pan-African western Saldania Belt, South Africa. *Precam. Res.* 231, 218-235.
- Fromm, T., Planert, L., Jokat, W., Ryberg, T., Behrmann, J.H., Weber, M.H., Haberland, C., 2015. South Atlantic opening: a plume-induced breakup? *Geology* 43, 931-934.
- Gibson, S.A., Thompson, R.N., Day, J.A., Humphris, S.E., Dickin, A.P., 2005. Melt-generation processes associated with the Tristan mantle plume: constraints on the origin of EM-1. *Earth Planet. Sci. Lett.* 237, 744-767.
- Gibson, S.A., Thompson, R.N., Day, J.A., 2006. Timescales and mechanisms of plume–lithosphere interactions: $^{40}\text{Ar}/^{39}\text{Ar}$ geochronology and geochemistry of alkaline igneous rocks from the Paraná–Etendeka large igneous province. *Earth Planet. Sci. Lett.* 251, 1-17.
- Gladchenko, T.P., Skogseid, J., Eldhom, O., 1998. Namibia volcanic margin. *Mar. Geophys. Res.* 20, 313-341.
- Goscombe, B., Gray, D.R., 2007. The Coastal Terrane of the Kaoko Belt, Namibia: outboard arc-terrane and tectonic significance. *Precam. Res.* 155, 139-158.
- Hart, S.R., 1984. A large-scale isotope anomaly in the southern hemisphere mantle. *Nature* 309, 753-757.
- Heine, C., Zoethout, J., Müller, R.D., 2013. Kinematics of the South Atlantic rift. *Solid Earth* 4, 215-253.
- Hoernle, K., Rohde, J., Hauff, F., Garbe-Schönberg, D., Homrighausen, S., Werner, R., Morgan, J.P., 2015. How and when plume zonation appeared during the 132 Myr evolution of the Tristan hotspot. *Nature Comm.* 6, 7799. doi: 10.1038/ncomms8799.
- Hoernle, K., Schwindrofska, A., Werner, R., van den Bogaard, P., Hauff, F., Uenzelmann-Neben, G., 2016. Tectonic dissection and displacement of parts of Shona hotspot volcano 3500 km along the Agulhas-Falkland Fracture Zone. *Geology* 44, 263-266.

- Iwamori, H., Nakamura, H., 2015. Isotopic heterogeneity of oceanic, arc and continental basalts and its implications for mantle dynamics. *Gondwana Res.* 27, 1131-1152.
- Janasi, V.A., de Freitas, V.A., Heaman, L.H., 2011. The onset of flood basalt volcanism, northern Paraná Basin, Brazil: a precise U-Pb baddeleyite/zircon age for a Chapecó-type dacite. *Earth Planet. Sci. Lett.* 302, 147-153.
- Jung, S., Mezger, K., Nebel, O., Kooijman, E., Berndt, J., Hauff, F., Münker, C., 2012. Origin of Meso-Proterozoic post-collisional leucogranite suites (Kaokoveld, Namibia): constraints from geochronology and Nd, Sr, Hf, and Pb isotopes. *Contrib. Mineral. Petrol.* 163, 1-17.
- Keiding, J.K., Frei, O., Renno, A.D., Veksler, I.V., Trumbull, R.B., 2013. Conditions of magma crystallization in the Henties Bay-Outjo dyke swarm, Namibia: implications for the feeder system of continental flood basalts. *Lithos* 179, 16-27.
- Kirstein, L.A., Kelley, S., Hawkesworth, C., Turner, S., Mantovani, M., Wijbrans, J., 2001. Protracted felsic magmatic activity associated with the opening of the South Atlantic. *J. Geol. Soc. London* 158, 583-592.
- Konopásek, J., Košler, J., Sláma, J., Janoušek, V., 2014. Timing and sources of pre-collisional Neoproterozoic sedimentation along the SE margin of the Congo Craton (Kaoko Belt, NW Namibia). *Gondwana Res.* 26, 386-401.
- Konopásek, J., Sláma, J., Košler, J., 2016. Linking the basement geology along the Africa-South America coasts in the South Atlantic. *Precam. Res.* 280, 221-230.
- Koopmann, H., Schreckenberger, B., Franke, D., Becker, K., Schnabel, M., 2014. The late rifting phase and continental break-up of the southern Atlantic: the mode and timing of volcanic rifting and formation of earliest oceanic crust. In: Wright, T.J., Ayele, A., Ferguson, D.J., Kidane, T., Vye-Brown, C. (Eds.), *Magmatic rifting and active volcanism*. *Geol. Soc. London Spec. Publ.* vol. 420, doi 10.1144/SP420.2
- Lee, J.-Y., Marti, K., Severinghaus, J.P., Kawamura, K., Yoo, H.-S., Lee, J.B., Kim, J.S., 2006. A redetermination of the isotopic abundances of atmospheric Ar. *Geochim. Cosmochim. Acta* 70, 4507–4512.
- le Roex, A., Class, C., 2014. Metasomatism of the Pan-African lithospheric mantle beneath the Damara Belt, Namibia, by the Tristan mantle plume: geochemical evidence from mantle xenoliths. *Contrib. Mineral. Petrol.* 168, 1046. doi 10.1007/s00410-014-1046-y
- le Roex, A.P., Cliff, R.A., Adair, B.J.I., 1990. Tristan da Cunha, South Atlantic: geochemistry and petrogenesis of a basanite-phonolite lava series. *J. Petrol.* 31, 779-812.

- le Roex, A., Class, C., O'Connor, J., Jokat, W., 2010. Shona and Discovery aseismic ridge systems, South Atlantic: trace element evidence for enriched mantle sources. *J. Petrol.* 51, 2089-2120.
- Ludwig, K.R., 2008. Isoplot 3.70. A Geochronological Toolkit for Microsoft Excel. Berkeley Geochron. Cent. Spec. Publ. vol. 4, 1-76.
- Marsh, J.S., Ewart, A., Milner, S.C., Duncan, A.R., Miller, R.McG., 2001. The Etendeka Igneous Province: magma types and their stratigraphic distribution with implications for the evolution of the Paraná-Etendeka flood basalt province. *Bull. Volcanol.* 62, 464-486.
- Marzoli, A., Melluso, L., Morra, V., Renne, P.R., Sgrosso, I., S'Antonio, M., Duarte Morais, L., Morais, E.A.A., Ricci, G., 1999. Geochronology and petrology of Cretaceous basaltic magmatism in the Kwanza basin (western Angola), and relationships with the Paraná-Etendeka continental flood basalt province. *J. Geodyn.* 28, 341-356.
- Maystrenko, Y.P., Scheck-Wenderoth, M., Hartwig, A., Anka, Z., Watts, A.B., Hirsach, K.K., Fishwick, S., 2013. Structural features of the southwest African continental margin according to results of lithosphere-scale 3D gravity and thermal modelling. *Tectonophysics* 604, 104-121.
- McDonough, W.F., Sun, S.S., 1995. The composition of the earth. *Chem. Geol.* 120, 223-253.
- Miller, R.Mc.G., 2008. Neoproterozoic and early Palaeozoic rocks of the Damara Orogen. In: Miller, R.Mc.G., (Ed.), *The Geology of Namibia, Volume 1*. Ministry of Mines. Geological Survey of Namibia, Windhoek, 13-1 – 13-410.
- Milner, S.C., le Roex, A.P., O'Connor, J.M., 1995. Age of Mesozoic igneous rocks in northwestern Namibia, and their relationship to continental breakup. *J. Geol. Soc. London* 152, 97-104.
- Mohriak, W., Nemčok, M., Enciso, G., 2008. South Atlantic divergent margin evolution: rift-border uplift and salt tectonics in the basis of SE Brazil. In: Pankhurst, R.J., Trouw, R.A.J., Brito Neves, B.B., De Wit, M.J. (Eds.), *West Gondwana: Pre-Cenozoic correlations across the South Atlantic region*. *Geol. Soc. London Spec. Publ.* vol. 294, 365-398.
- O'Connor, J.M., Duncan, R.A., 1990. Evolution of the Walvis Ridge-Rio Grande Rise hot spot system: implications for African and South American plate motions over plumes. *J. Geophys. Res.* 95, 17475-17502.
- O'Connor, J.M., le Roex, A.P., 1992. South Atlantic hot spot-plume systems: 1. Distribution of volcanism in time and space. *Earth Planet. Sci. Lett.* 113, 343-364.

- O'Connor, J.M., Jokat, W., 2015. Age distribution of ocean drill sites across the central Walvis Ridge indicates plate boundary control of plume volcanism in the South Atlantic. *Earth Planet. Sci. Lett.* 424, 179-190.
- O'Connor, J.M., Jokat, W., le Roex, A., Class, C., Wijbrans, J., Kessling, S., Kuiper, K., Nebel, O., 2012. Hotspot trails in the South Atlantic controlled by plume and plate tectonic processes. *Nat. Geosci.* 5, 735-738.
- Pearce, J.A., 1996. A user's guide to basalt discrimination diagrams. *Geol. Assoc. Canada Spec. Publ.* vol. 12, 79-113.
- Pearce, J.A., Peate, D.W., 1995. Tectonic implications of the composition of volcanic arc magmas. *Ann. Rev. Earth Planet. Sci.* 23, 251-285.
- Peate, D.W., 1997. The Paraná-Etendeka Province. In: Mahony, J.J., Coffin, M.F. (Eds.), *Large Igneous Provinces: Continental, Oceanic, and Planetary Flood Volcanism*. *Geophys. Mono.* vol. 100, 217-245.
- Pfänder, J.A., Sperner, B., Ratschbacher, L., Fischer, A., Meyer, M., Leistner, M., Schaeben, H., 2014. High-resolution $^{40}\text{Ar}/^{39}\text{Ar}$ dating using a mechanical sample transfer system combined with a high-temperature cell for step heating experiments and a multicollector ARGUS noble gas mass spectrometer. *Geochem. Geophys. Geosyst.* 15, 2713-2726.
- Renne, P.R., Deino, A.L., Walter, R.C., Turrin, B.D., Swisher, C.C., Becker, T.A., Curtis, G.H., Sharp, W.D., Jaouni, A.-R., 1994. Intercalibration of astronomical and radioisotopic time. *Geology* 22, 783-786.
- Renne, P.R., Glen, J.M., Milner, S.C., Duncan, A.R., 1996. Age of Etendeka flood volcanism and associated intrusions in southwestern Africa. *Geology* 24, 659-662.
- Renne, P.R., Deino, A.L., Hames, W.E., Heizler, M.T., Hemming, S.R., Hodges, K.V., Koppers, A.A.P., Mark, D.F., Morgan, L.E., Phillips, D., Singer, B.S., Turrin, B.D., Villa, I.M., Villeneuve, M., Wijbrans, J.R., 2009. Data reporting norms for $^{40}\text{Ar}/^{39}\text{Ar}$ geochronology. *Quat. Geochron.* 4, 346-352.
- Renne, P.R., Mundil, R., Balco, G., Min, K., Ludwig, K.R., 2010. Joint determination of ^{40}K decay constants and $^{40}\text{Ar}^*/^{40}\text{K}$ for the Fish Canyon sanidine standard, and improved accuracy for $^{40}\text{Ar}/^{39}\text{Ar}$ geochronology. *Geochim. Cosmochim. Acta* 74, 5349-5367.
- Richardson, S.H., Erlank, A.J., Duncan, A.R., Reid, D.L., 1982. Correlated Nd, Sr and Pb isotope variation in Walvis Ridge basalts and implications for the evolution of their mantle source. *Earth Planet. Sci. Lett.* 59, 327-342.

- Richardson, S.H., Erlank, A.J., Duncan, A.R., Reid, D.L., 1984. Major and trace elements and Nd and Sr isotope geochemistry of basalts from the Deep Sea Drilling Project Leg 74 Walvis Ridge transect. *Init. Repts. Deep Sea Drill. Proj.* 74, 739-754.
- Riley, T.A., Leat, P.T., Curtis, M.L., Millar, I.L., Duncan, R.A., Fazel, A., 2005. Early-Middle Jurassic dolerite dykes from western Dronning Maud Land (Antarctica): identifying mantle sources in the Karoo large igneous province. *J. Petrol.* 46, 1489-1524.
- Rocha-Júnior, E.R.V., Marques, L.S., Babinski, M., Nardy, A.J.R., Figueiredo, A.M.G., Machado, F.B., 2013. Sr-Nd-Pb isotopic constraints on the nature of the mantle sources involved in the genesis of the high-Ti tholeiites from northern Paraná continental flood basalts (Brazil). *J. South Am. Earth Sci.* 46, 9-25.
- Rohde, J.K., van den Bogaard, P., Hoernle, K., Hauff, F., Werner, R., 2013. Evidence for an age progression along the Tristan-Gough volcanic track from new $^{40}\text{Ar}/^{39}\text{Ar}$ ages on phenocryst phases. *Tectonophysics* 604, 60-71.
- Rudnick, R.L., Gao, S., 2003. Composition of the continental crust. In: Rudnick, R.L. (Ed.), *The crust. Treatise on geochemistry vol. 3*, 1-64.
- Ryberg, T., Haberland, C., Haberlau, T., Weber, M.W., Bauer, K., Behrmann, J.H., Jokat, W., 2015. Crustal structure of northwest Namibia: evidence for plume-rift-continent interaction. *Geology* 43, 739-742.
- Salters, V.J.M., Sachi-Kocher, A., 2010. An ancient source for the Walvis Ridge basalts. *Chem. Geol.* 273, 151-167.
- Späth, A., le Roex, A.P., Opiyo-Akech, N., 2001. Plume-lithosphere interaction and the origin of continental rift-related alkaline volcanism - the Chyulu Hills Volcanic Province, southern Kenya. *J. Petrol.* 42, 765-787.
- Seth, B., Kröner, A., Mezger, K., Nemchin, A.A., Pidgeon, R.T., Okrusch, M., 1998. Archaean to Neoproterozoic magmatic events in the Kaoko belt of NW Namibia and their geodynamic significance. *Precam. Res.* 92, 341-363.
- Steiger, R.H., Jäger, E., 1977. Subcommittee of geochronology: convention of the use of decay constants in geo- and cosmochemistry. *Earth Planet. Sci. Lett.* 36, 359-362.
- Stewart, K., Turner, S., Kelley, S., Hawkesworth, C., Kirstein, L., Mantovani, M., 1996. 3-D, ^{40}Ar - ^{39}Ar geochronology in the Paraná continental flood basalt province. *Earth Planet. Sci. Lett.* 143, 95-109.

- Sun, S.S., Mc Donough, W.F., 1989. Chemical and isotopic systematics of oceanic basalts: implications for mantle composition and processes. In: Saunders, A.D., Norry, M.J. (Eds.), *Magmatism in the ocean basins*. Geol. Soc. London Spec. Publ. vol. 42, 313-345.
- Thompson, G., Humphris, S.E., 1984. Petrology and geochemistry of rocks from the Walvis Ridge: Deep Sea Drilling Project Leg 74, Sites 525, 527, and 528. Initial Repts. Deep Sea Drill. Proj. 74, 755-764.
- Thompson, R.N., Gibson, S.A., 2000. Transient high temperatures in mantle plume heads inferred from magnesian olivines in Phanerozoic picrites. *Nature* 407, 502-506.
- Thompson, R.N., Gibson, S.A., Dickin, A.P., Smith, P.M., 2001. Early Cretaceous basalt and picrite dykes of the southern Etendeka region, NW Namibia: window into the role of the Tristan mantle plume in Paraná-Etendeka magmatism. *J. Petrol.* 42, 2049-2081.
- Thompson, R.N., Riches, A.J.V., Antoshechkina, P.M., Peasron, D.G., Nowell, G.M., Ottley, C.J., Dickin, A.P., Hards, V.L., Nguno, A.-K., Niku-Paavola, V., 2007. Origin of CFB magmatism: multi-tiered intracrustal picrite-rhyolite magmatic plumbing at Spitzkoppe, western Namibia, during Early Cretaceous Etendeka magmatism. *J. Petrol.* 48, 1119-1154.
- Tian, W., Campbell, I.H., Allen, C.M., Guan, P., Pan, W., Chen, M., Yu, H., Zhu, W., 2010. The Tarim picrite-basalt-rhyolite suite, a Permian flood basalt from northwest China with contrasting rhyolites produced by fractional crystallization and anatexis. *Contrib. Mineral. Petrol.* 160, 407-425.
- Torsvik, T.H., Rousse, S., Labails, C., Smethurst, M.A., 2009. A new scheme for the opening of the South Atlantic Ocean and the dissection of an Aptian salt basin. *Geophys. J. Int.* 177, 1315-1333.
- Trumbull, R.B., Vietro, T., Hahne, K., Wackerle, R., Ledru, P., 2004. Aeromagnetic mapping and reconnaissance geochemistry of the early Cretaceous Henties Bay-Outjo dike swarm, Etendeka igneous province, Namibia. *J. Afr. Earth Sci.* 40, 17-29.
- Trumbull, R.B., Reid, D.L., de Beer, C., van Acken, D., Romer, R.L., 2007. Magmatism and continental breakup at the west margin of southern Africa: a geochemical comparison of dolerite dikes from northwestern Namibia and the Western Cape. *South Afr. J. Geol.* 110,
- Turner, S., Regelous, M., Kelley, S., Hawkesworth, C., Mantovani, M., 1994. Magmatism and continental break-up in the South Atlantic: high precision $^{40}\text{Ar}/^{39}\text{Ar}$ geochronology. *Earth Planet. Sci. Lett.* 121, 333-348.

- Wang, K., Plank, T., Walker, J.D., Smith, E.I., 2002. A melting profile across the Basin and Range, SW USA. *J. Geophys. Res.* 107, doi: 10.1029/2001JB000209.
- Will, T.M., Frimmel, H.E., 2013. The influence of inherited structures on dike emplacement during Gondwana breakup in southwestern Africa. *J. Geol.* 121, 455-474.
- Will, T.M., Miller, R.M., Frimmel, H.E., 2009. Orogenic tectono-thermal evolution of the Kaoko Belt. In: Gaucher, C., Sial, A.N., Halverson, G.P., Frimmel, H.F. (Eds.), *Neoproterozoic-Cambrian tectonics, global change and evolution. A focus on southwestern Gondwana. Developments in Precambrian Geology*, Elsevier, Amsterdam, vol. 16, pp. 205-218.
- Will, T.M., Frimmel, H.E., Zeh, A., le Roux, P., Schmädicke, E., 2010. Geochemical and isotopic constraints on the tectonic and crustal evolution of the Shackleton Range, East Antarctica, and correlation with other Gondwana crustal segments. *Precam. Res.* 180, 85-112.
- Will, T.M., Frimmel, H.E., Gaucher, C., Bossi, J., 2014. Geochemical and isotopic composition of Pan-African metabasalts from southwestern Gondwana: evidence of Cretaceous South Atlantic opening along a Neoproterozoic back-arc. *Lithos* 202-203, 363-381.

Figure captions

Fig. 1. (a) Approximate location of the easternmost segment of the Walvis Ridge in the eastern South Atlantic and its onshore continuation along the NW Namibian coast. The Walvis Ridge samples analysed by Rohde et al. (2013) are dredge samples with mainly alkaline compositions. The DSDP Leg 74 drilling sites are approximately located at 29°04' S and 02°59' E. (b) Dyke and sampling locations in the study area between Terrace and Möwe Bay.

Fig. 2. Photomicrographs of Möwe Bay dolerite samples, cross-polarised light. Horizontal width of the photographs is 2.3 mm except for (e) that is 0.57 mm wide. (a) Fine-grained Type 1 sample N13-10. (b) Olivine-bearing and clinopyroxene- and plagioclase-phyric Type 2 sample N13-21 with rounded olivine grains. (c) Large plagioclase phenocrysts in coarse-grained Type 3 sample N13-7. (d) Recrystallised clinopyroxene grains in Type 3 sample N11-13. (e) Myrmekitic quartz-plagioclase intergrowth in Type 1 sample N13-25. (f) Radial plagioclase aggregates in Type 1 sample N13-11.

Fig. 3. Measured strike orientation data of Type 1 and 2 (top) and Type 3 dolerite dykes (bottom) in the Möwe Bay area (n = number of dykes).

Fig. 4. (a) Nb/Y-Zr/TiO₂ classification diagram (after Pearce, 1996), (b) Mg# versus TiO₂ plot.

Fig. 5. Trace element patterns of dolerite dykes from the Möwe Bay area, NW Namibia. (a-d) Type 1 dyke, (e-f) Type 2 dyke, (g-h) Type 3 dyke. (n = number of samples). Normalisation values and the values for the UCC (upper continental crust), OIB (ocean island basalt) and E-MORB (enriched mid-ocean ridge basalt) reference

curves are from Rudnick and Gao (2003) and Sun and McDonough (1989), respectively.

Fig. 6. Slope of light REE, $(La/Sm)_{cn}$, versus $(Pb/Pb^*)_{pm} = Pb_{pm}/\sqrt{(Ce_{pm} \cdot Pr_{pm})}$, a measure of Pb enrichment and/or depletion (relative to Ce and Pr).

Fig. 7. (a) Present-day $^{87}Sr/^{86}Sr - ^{143}Nd/^{144}Nd$, and (b) present-day $^{206}Pb/^{204}Pb$ versus $^{207}Pb/^{204}Pb$ diagrams of the Möwe Bay dolerite dykes; the northern hemisphere reference line, NHRL (Hart, 1984) and the EM1 (enriched mantle 1 end-member component) composition (Iwamori and Nakamura, 2015) are shown for reference. The μ_2 -values of 9.97 and 9.35 were determined according to Jung et al. (2012); r – correlation coefficient. Walvis Ridge isotope and age data are from Salters and Sochi-Kocher (2010), Rohde et al. (2013), O'Connor and Jokat (2015) and Hoernle et al. (2015). (c) The Type 1 and 2 samples plot on a straight line that runs through the average Kalahari Craton Pb isotope composition of Jung et al. (2012) indicated by the grey circle. The Damara A-type granite field in (a) is from Thompson et al. (2007); the field of S-type granites and metasedimentary Damara basement rocks plot to the lower right-hand side of the diagram. The Tristan da Cunha, Walvis Ridge (cross-hatched signature) and Damara basement compositional fields in (b) are drawn after Rocha-Júnior et al. (2013), le Roex and Class (2014) and Thompson et al. (2007), respectively.

Fig. 8. $^{40}Ar/^{39}Ar$ whole rock age spectra and inverse isochron diagrams. WMA - weighted mean age.

Fig. 9. Discrimination diagrams for dolerite dykes from the Möwe Bay area. (a) $Nb/Yb-Th/Yb$ (Pearce and Peate, 1995), (b) $(Nb/Nb^*)_{pm}-MgO$, (c) $(Nb/Nb^*)_{pm}-Ce/Pb_{pm}$, (d) $(Tb/Nb^*)_{pm}-MgO$, (e) $Ba/Nb-(Ce/Pb^*)_{pm}$ (le Roex et al., 2010). $(Ce/Pb)_{pm}$

of > 1.0 (Tian et al., 2010) and $(\text{Tb/Nb}^*)_{\text{pm}}$ of > 1.8 (Wang et al., 2002) are thought to be typical for plume-derived melts, respectively. The vertical line in (e) represents the maximum Ba/Nb ratio typically found in OIB (le Roex et al., 2010). PM: primitive mantle, OIB: ocean island basalt, E-MORB: enriched mid-ocean ridge basalt, UCC: upper continental crust, LCC: lower continental crust (the PM value is from McDonough and Sun (1995), other data sources as in caption to Fig. 5).

Appendix

$^{40}\text{Ar}/^{39}\text{Ar}$ analyses were carried out at Argonlabor Freiberg (ALF), TU Freiberg, Germany. Handpicked ground mass fragments up to ~1 mm in size were selected and washed repeatedly in deionised water using an ultrasonic bath to remove dust. After washing and drying, the rock chips were wrapped in Al foil and loaded into wells on Al discs (33 mm diameter) for irradiation, which was done for 6.5 hours at the LVR-15 research reactor of the Nuclear Research Institute in Řež, Czech Republic. The thermal neutron flux was $\sim 8 \times 10^{13} \text{ n/cm}^2\text{s}$ at a thermal to fast neutron ratio of ~1.1. Irradiated samples were unwrapped and loaded into small Mo-crucibles for furnace step heating experiments. Step heating was performed using a Createc® high-temperature cell (HTC) controlled by an Eurotherm 3504 controller (for details, see Pfänder et al., 2014). Gas purification was achieved by two GP50 getter pumps, one at room temperature and one at 400°C. Heating time was 7 minutes, cleaning time was 10 minutes per step. Argon isotope compositions were measured in static mode on a GV Instrument ARGUS noble gas mass spectrometer equipped with five faraday cups and 10^{12} Ohm resistors on mass positions 36-39 and a 10^{11} Ohm resistor on mass position 40. Typical blank levels are $2.5 \times 10^{-16} \text{ mol } ^{40}\text{Ar}$ and $8.1 \times 10^{-18} \text{ mol } ^{36}\text{Ar}$. Measurement time was 7.5 minutes per temperature step acquiring 45 scans at 10 seconds integration time each. Mass bias was corrected assuming linear mass dependent fractionation and using an atmospheric $^{40}\text{Ar}/^{36}\text{Ar}$ ratio of 298.6 ± 0.3 (Lee et al., 2006). For raw data reduction and time-zero intercept calculation an in-house developed Matlab® toolbox was used, isochron, inverse isochron and weighted mean ages were calculated using ISOPLOT 3.7 (Ludwig et al., 2008). All ages were calculated against Fish Canyon sanidine as flux monitor ($28.305 \pm 0.036 \text{ Ma}$; Renne et al., 2010), reported errors on ages are 1σ . Interference correction

factors are given as supplementary data, along with the raw data of Ar isotope measurements.

Figure 1

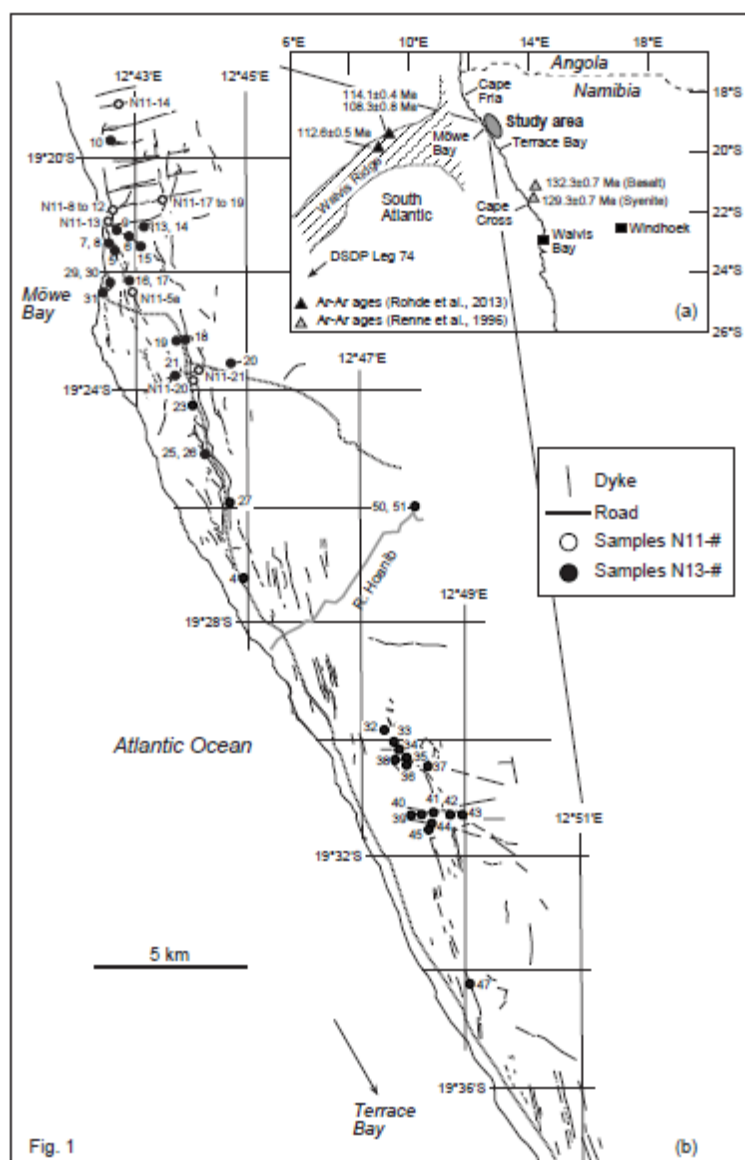


Figure 2

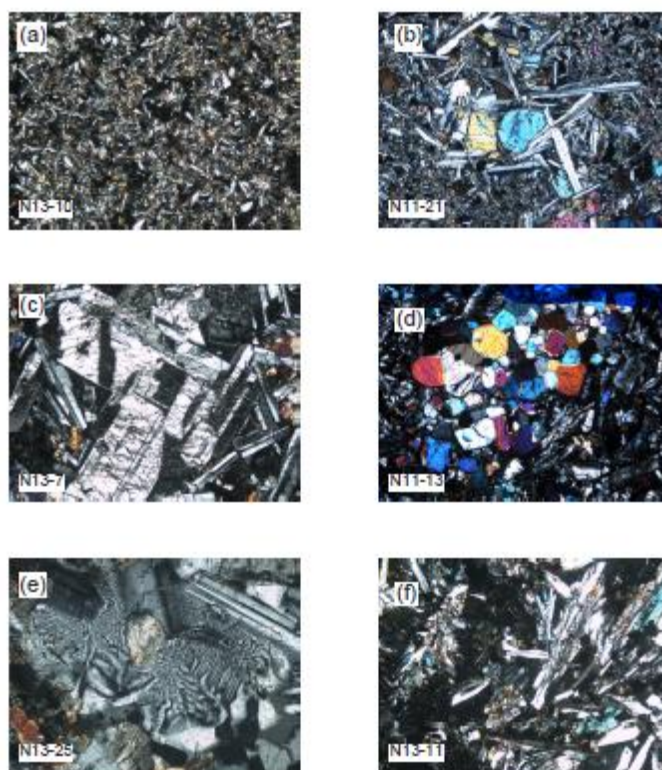


Fig. 2

Figure 3

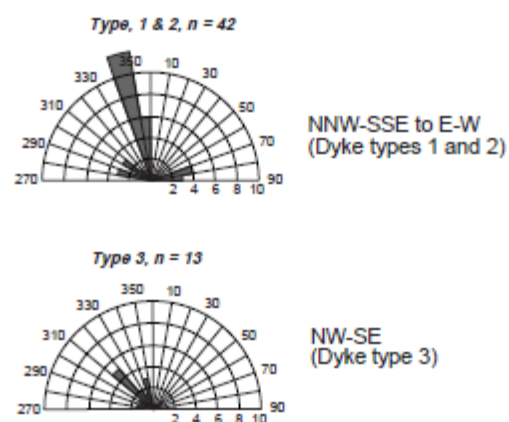


Fig. 3

Figure 4

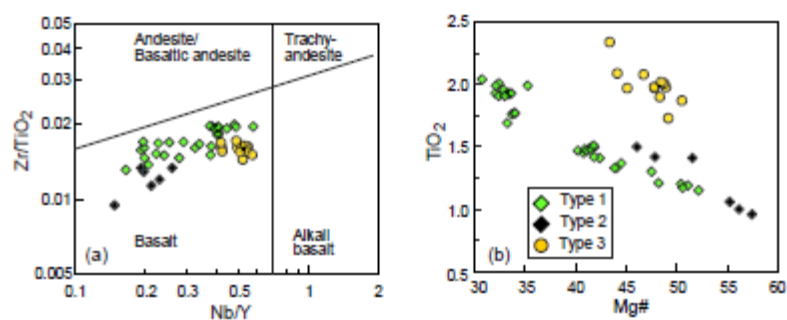


Fig. 4

Fig. 5

Figure 6

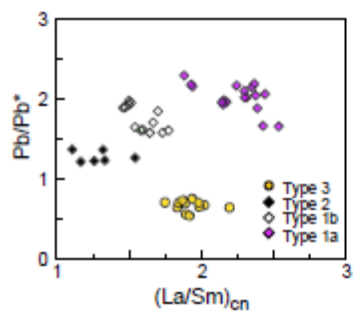


Fig. 6

Figure 7

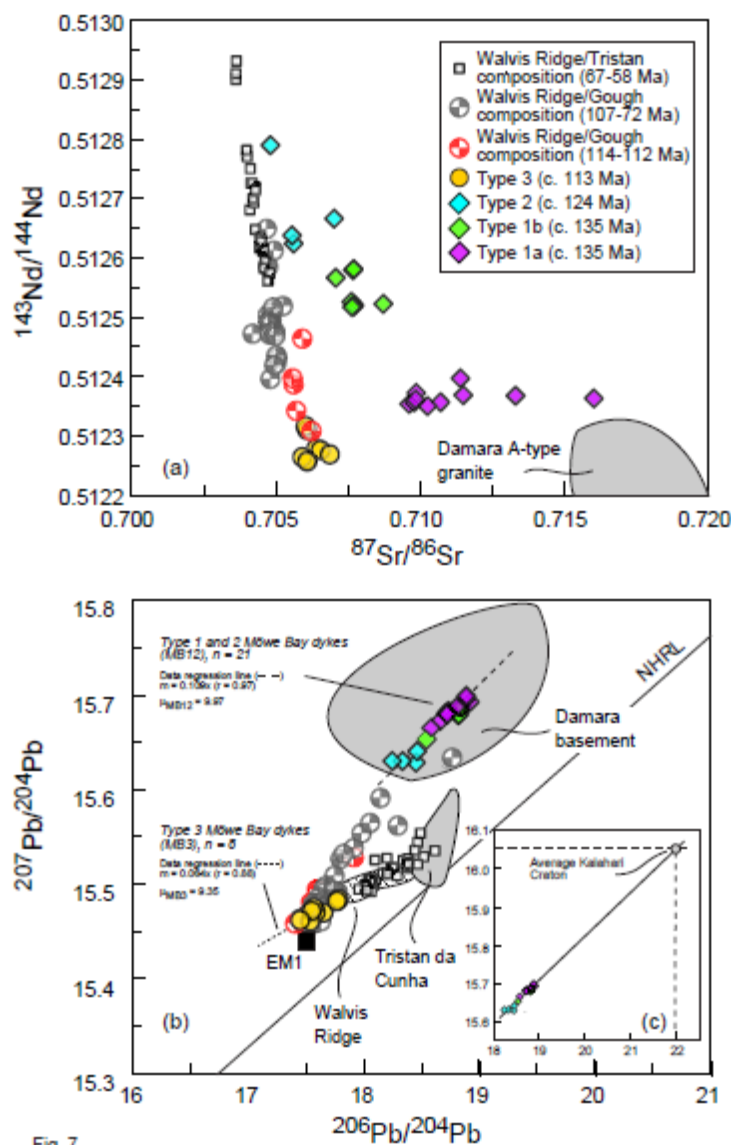


Fig. 7

Figure 8

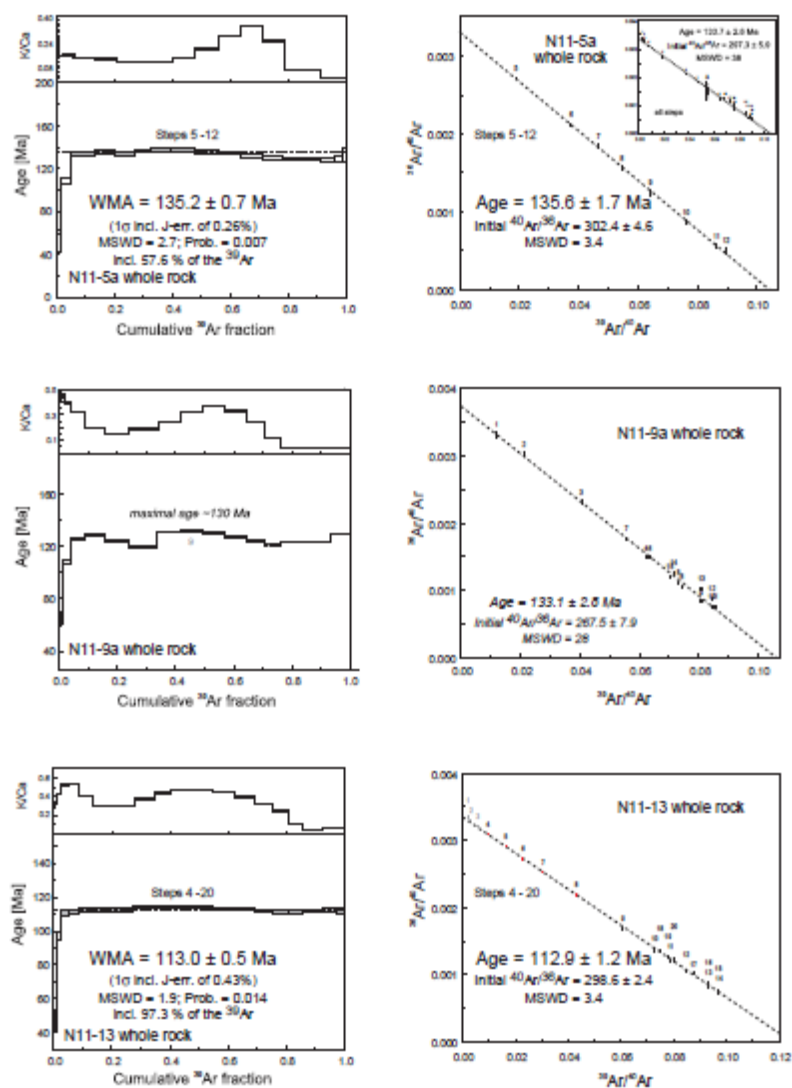


Fig. 8

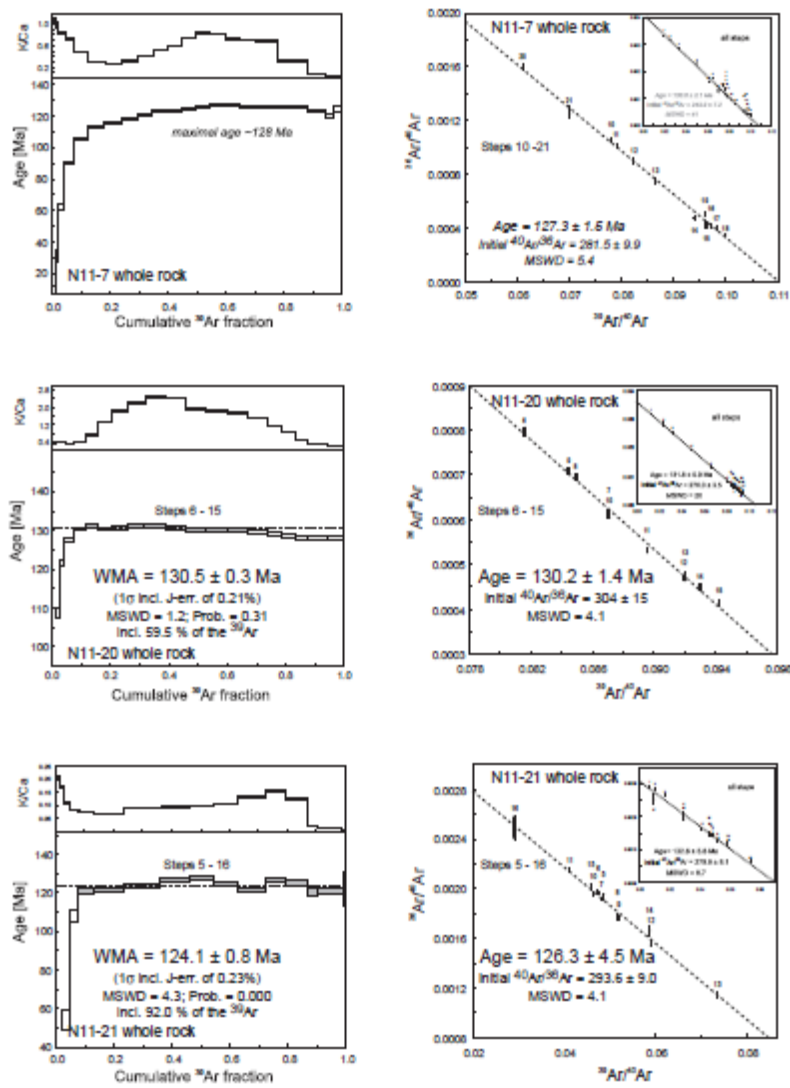


Fig. 8 (cont'd)

Figure 9

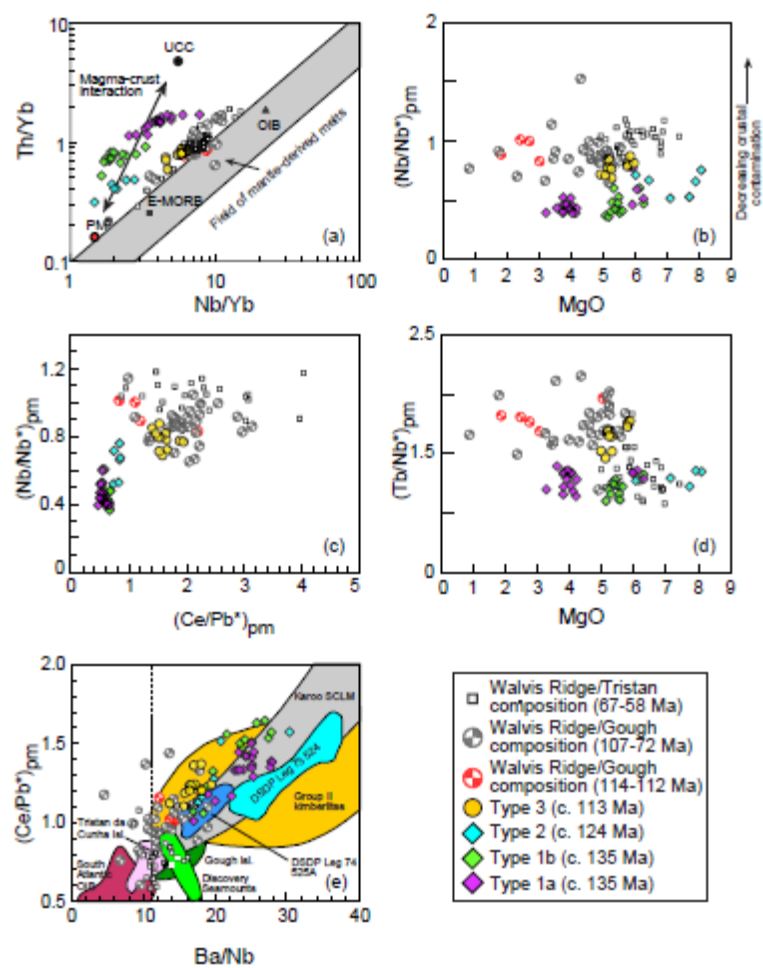


Fig. 9

N13-18	19°23'12.6	12°43'54.3	018°	1	X	X	X	X	X
N13-19	19°23'13.0	12°43'45.7	350°	1	X	X			
N13-20a	19°23'32.4	12°44'41.1	070°	2	X	X	X	X	X
N13-21	19°23'43.0	12°43'49.4	270°	2	X	X			
N13-23	19°24'08.0	12°43'59.6	350°	1	X	X	X	X	X
N13-25	19°25'06.1	12°44'15.4	012°	1	X	X			
N13-26	19°25'06.1	12°44'15.4	310°	1	X	X			
N13-27	19°25'50.7	12°44'39.9	350°	1	X	X	X	X	X
N13-29	19°22'12.9	12°42'33.7	024°	1	X	X			
N13-30a	19°22'12.9	12°42'33.7	345°	1	X	X	X	X	X
N13-31	19°22'23.2	12°42'24.6	342°	1	X	X	X	X	X
N13-32	19°29'49.2	12°47'30.9	320°	3	X	X	X	X	X
N13-33	19°30'00.1	12°47'40.1	320°	3	X	X			
N13-34	19°30'09.4	12°47'46.7	350°	3	X	X	X	X	X
N13-35	19°30'16.4	12°47'51.8	301°	1	X	X			
N13-36	19°30'23.6	12°47'57.2	314°	1	X	X	X	X	X
N13-38	19°30'20.7	12°47'43.4	300°	1	X	X	X	X	X
N13-39	19°31'19.0	12°48'02.9	080°	1	X	X	X	X	X
N13-40b	19°31'18.0	12°48'14.3	080°	1	X	X			
N13-41	19°31'15.8	12°48'24.2	080°	1	X	X			
N13-42	19°31'17.4	12°48'41.9	350°	1	X	X			
N13-43a	19°31'14.3	12°48'50.7	325°	3	X	X			
N13-44	19°31'29.4	12°48'24.6	290°	3	X	X			
N13-45	19°31'33.9	12°48'20.0	070°	1	X	X			
N13-47	19°34'28.5	12°49'11.2	350°	3	X	X	X	X	X
N13-49	19°35'05.6	12°50'15.2	325°	3	X	X	X	X	X
N13-50	19°26'00.5	12°48'02.6	300°	2	X	X	X	X	X

N13-51	19°26'00.5	12°48'02.6	303°	2	X	X
	"	"				

ACCEPTED MANUSCRIPT

Table 2. Summary of Sm-Nd whole rock isotope data from mafic dolerite dykes from Möwe Bay, Skeleton Coast, NW Namibia.

Sample	Dyke	Assumed	Sm	Nd	Sm/Nd	$^{143}\text{Nd}/^{144}\text{Nd}$	$\pm 2\sigma$	$^{147}\text{Sm}/^{144}\text{Nd}$	ϵ_{Nd}	$^{143}\text{Nd}/^{144}\text{Nd}$
	type	age, t (Ma)	(ppm)	(ppm)		measured	internal	calculated	today	initial at t
N11-17	1a	135	7.0	29	0.25	0.512354	8	0.14824	-5.54	0.51222
N11-19	1a	135	7.8	33	0.24	0.512357	10	0.14382	-5.48	0.51223
N11-20	1a	135	8.1	34	0.24	0.512363	9	0.14414	-5.36	0.51224
N13-4a	1a	135	6.7	29	0.24	0.512368	8	0.14189	-5.27	0.51224
N13-18	1a	135	6.9	28	0.24	0.512372	8	0.14569	-5.19	0.51224
N13-23	1a	135	7.1	30	0.24	0.512361	9	0.14316	-5.40	0.51224
N13-27	1a	135	6.8	28	0.24	0.512369	13	0.14586	-5.25	0.51224
N13-39	1a	135	5.5	22	0.26	0.512397	9	0.15450	-4.70	0.51226
N13-36	1a	135	4.1	18	0.23	0.512357	12	0.13739	-5.48	0.51224
N13-38	1a	135	4.3	19	0.23	0.512350	10	0.13833	-5.62	0.51223
N11-5a	1b	135	4.9	18	0.28	0.512520	9	0.16635	-2.30	0.51237
N11-8	1b	135	4.9	18	0.27	0.512522	8	0.16425	-2.26	0.51238
N11-9a	1b	135	4.3	15	0.29	0.512579	11	0.17235	-1.15	0.51243
N11-10	1b	135	4.3	15	0.29	0.512581	9	0.17726	-1.11	0.51242
N11-11	1b	135	4.4	15	0.29	0.512567	8	0.17620	-1.38	0.51241
N13-6a	1b	135	4.1	15	0.28	0.512526	7	0.17074	-2.18	0.51238
N13-16	1b	135	4.2	15	0.29	0.512519	11	0.17223	-2.32	0.51237
N13-30a	1b	135	4.1	15	0.28	0.512517	8	0.16866	-2.36	0.51237
N13-31	1b	135	4.0	14	0.29	0.512523	13	0.17357	-2.24	0.51237
N11-14	2	125	3.6	11	0.32	0.512790	10	0.19128	2.97	0.51263
N11-21	2	125	2.7	10	0.28	0.512624	9	0.16838	-0.27	0.51249
N13-20a	2	125	2.4	8.2	0.29	0.512638	11	0.17553	0.00	0.51249
N13-50	2	125	4.0	13	0.31	0.512666	9	0.18957	0.55	0.51251
N11-13	3	113	8.3	34	0.24	0.512279	11	0.14555	-7.00	0.51217
N13-5	3	113	5.8	24	0.24	0.512261	10	0.14233	-7.35	0.51216
N13-8	3	113	6.5	27	0.24	0.512276	9	0.14481	-7.06	0.51217
N13-9	3	113	6.1	26	0.24	0.512269	8	0.14342	-7.20	0.51216
N13-15	3	113	6.0	26	0.24	0.512264	10	0.14171	-7.30	0.51216
N13-32	3	113	5.9	24	0.24	0.512310	9	0.14668	-6.40	0.51220
N13-34	3	113	6.0	25	0.24	0.512317	9	0.14604	-6.26	0.51221
N13-47	3	113	6.2	26	0.24	0.512257	10	0.14314	-7.43	0.51215

All samples have $^{147}\text{Sm}/^{144}\text{Nd}$ ratios higher than 0.13, which may indicate that the Sm/Nd ratios were modified during the post-magmatic evolution of the rocks. Thus, the two-stage model of Keto and Jacobsen (1987) was used to calculate the Nd model ages presented in the last column (see Will et al., 2014, for details).

Table 3. Summary of Rb-Sr and Pb-Pb whole rock isotope data from mafic dolerite dykes from Möwe Bay, Skeleton Coast, NW Namibia.

Sample	Dyke type	Assumed age, t (Ma)	Rb (ppm)	Sr (ppm)	Rb/Sr	$^{87}\text{Sr}/^{86}\text{Sr}$ measured	$\pm 2\sigma$ internal	$^{87}\text{Sr}/^{86}\text{Sr}$ initial	U (ppm)	Pb (ppm)	Th (ppm)	U/Pb	Th/Pb	$^{208}\text{Pb}/^{204}\text{Pb}$	$\pm 2\sigma$ internal	$^{207}\text{Pb}/^{204}\text{Pb}$	$\pm 2\sigma$ internal	$^{206}\text{Pb}/^{204}\text{Pb}$	$\pm 2\sigma$ internal
N1-17	1a	135	39.5	25.4	0.154	0.70961	12	0.70875	1.35	7.03	5.75	0.119	0.081	38.8162	0.0021	15.6716	0.0008	18.6639	0.0007
N1-19	1a	135	41.65	25.975	0.1596	0.709789	13	0.70899	1.97	7.983	6.83	0.122	0.083	38.8736	0.0025	15.6821	0.0008	18.7378	0.0009
N1-20	1a	135	95.15	22.65	0.42421	0.71601	14	0.71367	4.00	8.898	6.75	0.145	0.076	38.976	0.0023	15.6917	0.0008	18.9234	0.0008
N1-3-4a	1a	135	91.2	27.9	0.329	0.71307	13	0.71108	1.35	8.425	5.45	0.167	0.067	38.8871	0.003	15.6798	0.0008	18.7179	0.0001
N1-3-18	1a	135	48.84	25.48	0.2025	0.709851	10	0.70853	1.38	8.49	5.5	0.168	0.068	38.7128	0.0024	15.6642	0.0003	18.5864	0.0007
N1-3-23	1a	135	52.8	26.4	0.2128	0.709839	14	0.70848	1.35	8.673	5.73	0.161	0.061	38.8857	0.0027	15.6798	0.0009	18.7238	0.0009
N1-3-27	1a	135	69.3	25.4	0.2735	0.709488	11	0.70958	1.34	8.44	5.9	0.166	0.066	38.8872	0.0026	15.6784	0.0006	18.7281	0.0008
N1-3-39	1a	135	49.0	26.3	0.2125	0.709402	13	0.70977	1.28	7.81	4.1	0.169	0.069	38.9085	0.0024	15.6873	0.0008	18.8173	0.0007
N1-3-36	1a	135	89.5	31.9	0.2796	0.710706	15	0.70977	1.09	5.89	3.7	0.178	0.068	38.922	0.003	15.6952	0.0006	18.8889	0.0001
N1-3-38	1a	135	72.7	29.2	0.2493	0.71025	13	0.70935	1.05	6.29	3.7	0.177	0.065	38.9289	0.0031	15.698	0.0012	18.8882	0.0011
N1-1-5a	1b	135	91.7	18.5	0.1114	0.70722	14	0.70715	0.74	3.70	2.78	0.132	0.073	38.8217	0.0024	15.6814	0.0008	18.7993	0.0001

N1	1	135	5	1	0.	0.7					0	0.	38.	0.	15.	0.	18.	0.
1-8	b		1	8.	9	07	13	0.7	0.	3.	2.	0	7	38.	0.	15.	0.	0.
			9	9	9	66		07	7	7	9	2	6	543	00	652	549	00
			5	3	8	9		12	7	7		1	9	5	2	4	7	06
N1	1	135	2	1	0.	0.7					0	0.	38.	0.	15.	0.	18.	0.
1-9a	b		5	1	1	07	12	0.7	0.	3.	2.	0	7	38.	0.	15.	0.	0.
			1	8	3	67		06	6	8	3	2	3	857	00	680	832	00
			2	8	4	3		93	6	5	3	1	2	6	27	2	09	08
N1	1	135	2	1	0.	0.7					2.	0	0.	38.	0.	15.	0.	0.
1-10	b		5	1	1	07	11	0.7	0.	3.	2.	0	7	38.	0.	15.	0.	0.
			4	9	3	69		06	6	1	4	2	2	839	00	677	818	00
			2	0	4	9		96	4		5	1	4	3	26	7	09	08
N1	1	135	2	1	0.	0.7					2.	0	0.	38.	0.	15.	0.	0.
1-11	b		5	1	1	07	12	0.7	0.	3.	2.	0	7	38.	0.	15.	0.	0.
			2	9	1	07		06	5	1	3	3	1	852	00	678	825	00
			0	1.	0	07		49	9	9	6	1	4	8	26		1	09
N1	1	135	2	1	0.	0.7					2.	0	0.	38.	0.	15.	0.	0.
3-6a	b		5	1	1	07	15	0.7	0.	3.	2.	0	7	38.	0.	15.	0.	0.
			1	5	1	07		06	6	6	3	1	2	885	00	686	841	00
			8	4.	4	62		84	4	7	1	7	9	3	34	7	10	1
N1	1	135	4	1	0.	0.7					2.	0	0.	38.	0.	15.	0.	0.
3-16	b		1	1	1	07	15	0.7	0.	3.	2.	0	6	38.	0.	15.	0.	0.
			1	4	1	07		06	6	8	3	1	2	883	00	686	843	00
			7	7.	4	68		86	9	1	9	1	2	2	3	3	09	1
N1	1	135	2	1	0.	0.7					2.	0	0.	38.	0.	15.	0.	0.
3-30	b		4	1	1	07	13	0.7	0.	3.	2.	0	6	38.	0.	15.	0.	0.
a			3	5.	3	63		06	6	7	3	1	1	878	00	685	848	00
			4	1	3	3		89	6	5	2	8	9	9	27	9	6	08
N1	1	135	3	1	0.	0.7					2.	0	0.	38.	0.	15.	0.	0.
3-31	b		0	5	0.	08	13	0.7	0.	3.	2.	0	6	38.	0.	15.	0.	0.
			9	4.	2	71		07	6	5	3	1	5	883	00	686	854	00
			1	5	9			61	4	3	3	8	2	1	31	7	09	09
N1	2	125	7	2	0.	0.7					0	0.	0.	38.	0.	15.	0.	0.
1-14			2	0	0	04	11	0.7	0.	1.	0.	0	4	38.	0.	15.	0.	0.
			4	3.	3	80		04	2	7	8	1	5	53	00	627	454	00
			5	5	6	9		63	1	6	0	1	6	27	7	09	8	08
N1	2	125	6	2	0.	0.7					0	0.	0.	38.	0.	15.	0.	0.
1-21			4	0	0	05	13	0.7	0.	1.	0.	0	5	38.	0.	15.	0.	0.
			4	5.	3	60		05	1	5	8	1	2	599	00	629	18.	00
			8	5	1	9		45	9	5	4	2	4	8	23	3	08	08
N1	2	125	3	1	0.	0.7					0	0.	0.	38.	0.	15.	0.	0.
3-20			1	6	0	05	13	0.7	0.	1.	0.	0	5	38.	0.	15.	0.	0.
a			1	9.	3	56		05	1	2	7	1	6	627	00	629	250	00
			6	8	5	5		39	6	4		3	5	3	38		13	16
N1	2	125	1	1	0.	0.7					0	0.	0.	38.	0.	15.	0.	0.
3-50			8	6	1	07	15	0.7	0.	2.	1.	0	5	38.	0.	15.	0.	0.
			2	7.	0	00		06	3	1	1	1	3	620	00	639	465	00
			5	6	9	8		45	2	1	3	5	6	3	28	6	09	12
N1	3	113	2	4	0.	0.7					2.	0	0.	38.	0.	15.	0.	0.
1-13			6	1	0	06	12	0.7	0.	3.	2.	0	8	38.	0.	15.	0.	0.
			9	1	6	4		06	5	8	8	1	3	413	00	470	652	00
			5	1	6			1	4	8	3	8	6	2	21	3	07	07
N1	3	113	4	3	0.	0.7					2.	1.	0	38.	0.	15.	0.	0.
3-5			1	1	0	06	14	0.7	0.	2.	1.	0	8	38.	0.	15.	0.	0.
			1	7.	5	10		05	2	3	9	1	2	194	00	470	584	00
								87	9	7	5			3	35	7	11	08

			3	8	1						2	3				3		
			5															
N1			2	3	0.	0.7						0.				0.	17.	0.
3-			3.	6	0	06						9	38.	0.	15.	00	782	00
8	3	113	8	9.	6	55	18	06	4	1	1	.	481	00	484	10	2	11
			6	7	5	6		26	3	3	2	2	5	36	2	6		
N1			2	3	0.	0.7						0	1.			0.	17.	0.
3-			4.	8	0	06						.	0			00	766	00
9	3	113	2	2.	6	86	11	06	4	9	0	.	472	00	482	10	3	1
			4	5	3	5		57	2	3	1	2	4	38	4	2		
			4									2	1					
N1			0	3	0.	0.7						0	0.			0.	17.	0.
3-			9	7	0	05						.	7			00	538	00
15	3	113	8	1.	3	92	14	05	2	6	9	1	306	00	460	10	3	1
			0	9	6			75	9	9	9	1	4	6	33	1		
			4									0	0.					
N1			1	3	0.	0.7						0	0.			0.	17.	0.
3-			0	1	0	06						.	8			00	567	00
32	3	113	1	6.	4	07	12	05	3	1	7	1	243	00	475	10	3	1
			2	5	5	9		87	9	7	7	8	6	32	2	5		
			1									0	0.					
N1			5.	3	0	06						.	7			00	17.	0.
3-			6	6.	4	02						1	3			10	550	00
34	3	113	6	5	7	2	16	05	4	4	8	6	235	00	472	2	7	11
			6					81	0	4		8	6	3				
			1	3	0.	0.7						0	0.			0.	17.	0.
N1			6.	1	0	06						.	7			00	450	00
3-			5	2.	5	08						1	5			12	2	13
47	3	113	9	7	3	7	14	05	4	6	2	5	129	00	462	9		
								84	1	6		2	9	4	1			

Table 4. $^{40}\text{Ar}/^{39}\text{Ar}$ ages.

Sa m pl e	Ex p. N o.	TG A [M a]	W MA [Ma]	M S W D	St e p s	% 3 9 Ar	W MA [Ma]	IIA [M a]	($^{40}\text{Ar}/^{36}\text{Ar}$) _i	M S W D	St e p s	IIA [M a]	($^{40}\text{Ar}/^{36}\text{Ar}$) _i	M S W D	St e p s	Comments
							rec alc.	inverse isochron data of plateau steps				inverse isochron data of all steps				
N 11			135		5		133	135	302		5	133	297			Some Ar loss on the low T steps
-	71	13	.2 ±	2.	1	7.	.0 ±	.6 ±	.4 ±	3.	1	.7 ±	.3 ±		al	
5a	39	2.7	0.7	7	2	6	0.7	1.7	4.6	4	2	2.6	5.9	38	l	
N 11												<i>133</i>	<i>267</i>			Dominated by Ar loss Slightly disturbed age spectrum
-	71	12										<i>.1 ±</i>	<i>.5 ±</i>		al	
9a	28	4.4	--	--	--	--		--	--	--	--	2.8	7.9	28	l	
N 11			113		4		111	112	298		4	113	296			Significant Ar loss
-	71	11	.0 ±	1.	2	7.	.2 ±	.9 ±	.6 ±	3.	2	.4 ±	.6 ±	9.	al	
13	24	1.7	0.5	9	0	3	0.5	1.2	2.4	4	0	1.2	1.9	1	l	
N 11												<i>130</i>	<i>243</i>			Some Ar loss
-	71	11										<i>.6 ±</i>	<i>.9 ±</i>		al	
17	21	7.5	--	--	--	--		--	--	--	--	2.1	7.2	41	l	
N 11			130		6		128	130	304		6	131	276			
-	71	12	.5 ±	1.	1	9.	.4 ±	.2 ±	±	4.	1	.8 ±	.0 ±		al	
20	10	8.3	0.3	2	5	5	0.3	1.4	15	1	5	0.9	3.5	26	l	
N 11																
-	71	11	124		5		122	126	293		5	132	279			
21	43	8.2	.1 ±	4.	1	2.	.1 ±	.3 ±	.6 ±	4.	1	.6 ±	.9 ±	8.	al	
			0.8	3	6	0	0.8	4.5	9.0	1	6	5.8	8.1	7	l	

All errors are 1s. Errors on plateau ages, where given, are weighted mean errors and commonly underestimate the external reproducibility which is in the order of $\pm 1\%$ (1s). Recommended ages are given in bold. Ages in italics are informal and represent disturbed samples. WMA = Weighed mean age, IIA = inverse isochron age. Reference age of the fluence monitor (Fish Canyon Tuff sanidine) = 28.305 ± 0.036 Ma (Renne et al., 2010). Decay constants used are from Renne et al. (2010). If not denoted otherwise in the corresponding figure, age spectra have been calculated applying an atmospheric $^{40}\text{Ar}/^{36}\text{Ar}$ of 298.6 ± 0.3 (Lee et al., 2006). WPA recalc. are plateau ages recalculated to a Fish Canyon Tuff sanidine age of 27.84 Ma (Renne et al. 1994) and the decay constant of Steiger & Jäger (1975) to permit a better comparison to literature values.

Graphical abstract

